



ChemComm

**Concerted Proton-Electron Transfer Reactions of
Manganese-Hydroxo and Manganese-Oxo Complexes**

Journal:	<i>ChemComm</i>
Manuscript ID	CC-FEA-02-2020-001201.R2
Article Type:	Feature Article

SCHOLARONE™
Manuscripts

ARTICLE

Concerted Proton-Electron Transfer Reactions of Manganese-Hydroxo and Manganese-Oxo Complexes

Jaycee R. Mayfield,^a Elizabeth N. Grotemeyer^a and Timothy A. Jackson^{a*}

Received 00th January 20xx,
Accepted 00th January 20xx

DOI: 10.1039/x0xx00000x

The enzymes manganese superoxide dismutase and manganese lipoxygenase use Mn^{III}-hydroxo centres to mediate proton-coupled electron transfer (PCET) reactions with substrate. As manganese is earth-abundant and inexpensive, manganese catalysts are of interest for synthetic applications. Recent years have seen exciting reports of enantioselective C–H bond oxidation by Mn catalysts supported by aminopyridyl ligands. Such catalysts offer economic and environmentally-friendly alternatives to conventional reagents and catalysts. Mechanistic studies of synthetic catalysts highlight the role of Mn-oxo motifs in attacking substrate C–H bonds, presumably by a concerted proton-electron transfer (CPET) step. (CPET is a subclass of PCET, where the proton and electron are transferred in the same step.) Knowledge of geometric and electronic influences for CPET reactions of Mn-hydroxo and Mn-oxo adducts enhances our understanding of biological and synthetic manganese centers and informs the design of new catalysts. In this Feature article, we describe kinetic, spectroscopic, and computational studies of Mn^{III}-hydroxo and Mn^{IV}-oxo complexes that provide insight into the basis for the CPET reactivity of these species. Systematic perturbations of the ligand environment around Mn^{III}-hydroxo and Mn^{IV}-oxo motifs permit elucidation of structure-activity relationships. For Mn^{III}-hydroxo centers, electron-deficient ligands enhance oxidative reactivity. However, ligand perturbations have competing consequences, as changes in the Mn^{III/II} potential, which represents the electron-transfer component for CPET, is offset by compensating changes in the pK_a of the Mn^{II}-aqua product, which represents the proton-transfer component for CPET. For Mn^{IV}-oxo systems, a multi-state reactivity model inspired the development of significantly more reactive complexes. Weakened equatorial donation to the Mn^{IV}-oxo unit results in large rate enhancements for C–H bond oxidation and oxygen-atom transfer reactions. These results demonstrate that the local coordination environment can be rationally changed to enhance reactivity of Mn^{III}-hydroxo and Mn^{IV}-oxo adducts.

Background

Manganese is an essential metal.¹ From the detoxification of free radicals in humans to the splitting of water to protons, electrons, and O₂ in plants, manganese-dependent enzymes perform a diverse range of reactions critical to life and intriguing from a fundamental perspective.^{2–5} A common theme among redox-active manganese enzymes is the participation of manganese-hydroxo and/or manganese-oxo species in proton-coupled electron-transfer (PCET) reactions.^{6–9} As a representative example, PCET reactions for manganese superoxide dismutase are shown in Figure 1.^{5, 10, 11} Both superoxide oxidation and reduction require electron transfer to and from the Mn centre, which shuttles between the Mn^{III} and Mn^{II} states. Changes in the Mn oxidation state are accompanied by changes in the protonation state of the coordinated solvent (OH₂ for Mn^{II} and OH[–] for Mn^{III}; see Figure 1). However, the extent to which electron transfer at the Mn centre is coupled with proton transfer at the solvent ligand is unclear.



Biographies

Jaycee Mayfield attended the University of Arkansas-Fort Smith for her undergraduate studies, and received her B.S. degree in chemistry with a concentration in biochemistry. She is currently a third-year graduate student at the University of Kansas and she is supported by the NIH Training Grant in Dynamic Aspects of

Chemical Biology. Her research focuses on understanding ligand field influences on the reactivity of Mn^{IV}-oxo species.

Liz Grotemeyer received her B.S degrees in Biochemistry and



Mathematics from California State University Dominguez Hills. She received her M.A in Biochemistry and Biophysics from the University of Kansas for her work evaluating proteasome assembly kinetics with Prof. Eric Deeds. Currently, Liz is a third-year graduate student in the Jackson lab where she studies Mn^{III}-hydroxo systems.

^a Department of Chemistry and Center for Environmentally Beneficial Catalysis, University of Kansas, Lawrence, KS 66045.

Tim Jackson received his B.S. degree in chemistry from St. Cloud State University. As a graduate student in Prof. Thomas Brunold's lab (University of Wisconsin-Madison), he performed spectroscopic and computational studies of Fe and Mn superoxide dismutases, earning his Ph.D. in 2004. He learned kinetic and synthetic methods as an NIH post-doctoral fellow in Prof. Lawrence Que Jr.'s lab (University of Minnesota). His independent research at the University of Kansas is focused on developing knowledge of transition-metal electronic structure to understand chemical reactivity. He is currently a Professor of Chemistry and Faculty Fellow of the University Honors program.

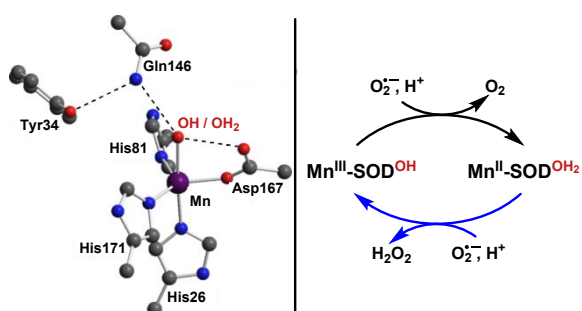
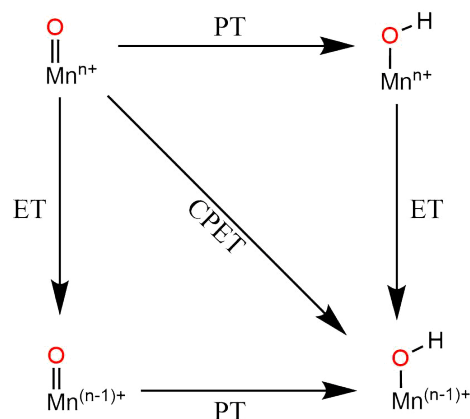


Figure 1. Left: Active-site of MnSOD, with the numbering scheme from *E. coli* (from pdb 1VEW). The solvent protonation state switches from OH⁻ for Mn^{III} to OH₂ for Mn^{II}. Dashed lines indicated hydrogen-bonds. Right: Ping-pong mechanism for superoxide disproportionation to O₂ and H₂O₂ observed for most MnSODs at low superoxide concentration. A red superscript marks the protonation state of coordinated solvent.

High-valent Mn-oxo adducts are also important intermediates for PCET reactions of biological and synthetic catalysts.^{7, 8, 12-15} Multinuclear manganese-oxo units play roles in the manganese ribonucleotide reductase (Mn-RNR) enzyme¹⁶ and the oxygen-evolving complex (OEC) of photosystem II.³ In Mn-RNR, activation of superoxide by a Mn^{II}Mn^{II} centre gives an oxo-bridged Mn^{III}Mn^{IV} species that oxidizes a nearby tyrosine residue as part of the preparatory steps for ribonucleotide reduction.¹⁶ High-valent, terminal Mn-oxo motifs are featured in some of the proposed mechanisms for water splitting and O–O bond formation in the OEC.^{3, 17-19} From synthetic chemistry, manganese catalysts supported by aminopyridyl ligands have shown great utility for C–H bond functionalization reactions.²⁰⁻²³ The ease of ligand modification in these systems offers advantages over porphyrin-based catalysts. While Mn^V-oxo adducts are the presumed oxidants for many of these aminopyridyl-based catalysts,^{21, 22} the characterization of *bona fide* Mn^V-oxo species in such ligand environments remains elusive.²⁴ Mn^{IV}-oxo adducts in similar ligand environments can also perform the oxidation of strong C–H bonds,^{25, 26} and some of these compounds show high thermal stability. One central question in PCET reactions of metal-oxo species is the relationship between geometric and electronic structure and reactivity, and the combination of stability and reactivity of Mn^{IV}-oxo adducts make them well-suited for such studies.

Combined experimental and computational approaches have illuminated the complexity of PCET reactions for a broad range of metal-based oxidants.^{27, 28} These reactions can occur in a single kinetic step by a concerted proton-electron transfer (CPET) or by a stepwise process (ETPT, electron-transfer followed by proton-transfer, or PTET, proton-transfer followed by electron-transfer; see Scheme 1).^{27, 29} CPET reactions often avoid high energy intermediates and are common for C–H bond oxidation by metal-oxo species. Present understanding of the nature of CPET reactions have been expanded by more recent reports of such reactions for metal-hydroxo, metal-carboxylate, and metal-superoxo complexes.³⁰



Scheme 1. Reaction diagram illustrating the difference between stepwise ETPT and PTET processes (edges) and CPET process (diagonal) for a generic Mnⁿ⁺-oxo species. The literature contains several distinctions between CPET and hydrogen-atom transfer (HAT) steps. While HAT is commonly, but not always, taken to mean transfer of an electron and proton from one donor to one acceptor, CPET can also encompass transfer of an electron to one donor and transfer of a proton to a separate donor (so-called multi-site concerted CPET, or MS-CPET). See ref. 27 for a deeper discussion of these terms. Alternatively, Hammes-Schiffer has distinguished these pathways on the basis of proton transfer occurring by an electronically adiabatic (HAT) or nonadiabatic (CPET) process.²⁹

Our contributions to this field have focused on defining the influences of geometric and electronic structure in modulating the CPET reactivity of Mn^{III}-hydroxo³¹⁻³³ and Mn^{IV}-oxo^{26, 34, 35} adducts. We have focused on supporting ligands that are easy to synthesize and amenable to modifications to perturb the steric and electronic environments of the Mn^{III}-hydroxo and Mn^{IV}-oxo units. The effects of these ligand variations are assessed by i) spectroscopic characterization of geometric and electronic structure of the Mn complex, ii) kinetic investigation of CPET reactivity, and iii) computational evaluation of key thermodynamic and kinetic properties, especially those challenging to obtain by experimental methods. In some cases ligand modifications have been informed by an analysis of computational predictions.³⁶ This work has led to new insights into the basis of reactivity of Mn^{III}-hydroxo and Mn^{IV}-oxo centres, which have importance for both biological and synthetic catalysts.

Manganese(III)-hydroxo complexes

In the oxidative half-reaction of MnSOD, an active-site Mn^{III}-hydroxo unit accepts an electron from O₂⁻ to give dioxygen

(Figure 1). A Mn^{III} -hydroxo adduct also plays a direct role in substrate oxidation in the enzyme manganese lipoxygenase (MnLOX).³⁷⁻⁴³ The proposed mechanism for this enzyme involves hydrogen-atom abstraction from the C–H bond of the polyunsaturated fatty acid substrate by a Mn^{III} -hydroxo adduct to give the corresponding Mn^{II} -aqua species and a carbon-centred radical (Figure 2). This step proceeds with a large, temperature-independent H/D kinetic isotope effect ($k_{\text{H}}/k_{\text{D}} = 20 - 24$).^{39, 40} Rearrangement of the substrate radical and subsequent reaction with O_2 leads to the formation of a substrate peroxy radical (Figure 2). The conversion of the peroxy radical to the hydroperoxy product has been postulated to occur by two different pathways. In one proposed pathway, the peroxy radical abstracts a hydrogen atom from the Mn^{II} -aqua species to give the organic product and regenerates the Mn^{III} -hydroxo unit (Figure 2).⁴⁴ Alternatively, the substrate peroxy radical displaces the aqua ligand to form a Mn^{III} -alkylperoxy adduct that is hydrolysed by water to yield the hydroperoxy product and the Mn^{III} -hydroxo resting state.⁹

Although several Mn-dependent enzymes feature Mn^{III} -hydroxo units, this motif has been rare in synthetic chemistry. In 2012 only seven structurally-characterized mononuclear Mn^{III} -hydroxo adducts had been reported.⁴⁵⁻⁵¹ Of these complexes, only one was known to mimic MnLOX in performing C–H bond oxidation reactions.⁴⁸

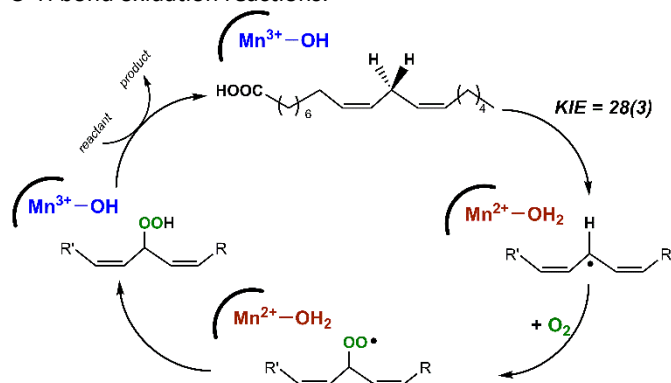


Figure 2. Schematic mechanism for substrate oxidation by manganese lipoxygenase. The substrate radical formed in the first step can rearrange to yield oxygenated product at a carbon different than the one indicated above (see ref⁴¹ and⁴²).

Formation and reactivity of a Mn^{III} -hydroxo adduct.

From this prior work on synthetic Mn^{III} -hydroxo centres, one prevailing notion was that steric bulk around the hydroxo ligand was needed to enforce mononuclearity by suppressing the formation of multinuclear hydroxo-bridged complexes. In fact, crystal structures of many Mn^{III} -hydroxo adducts displayed hydrogen-bonding to the hydroxo ligand^{46, 48, 50} and/or showed the supporting ligand providing steric shelter for the hydroxo.⁴⁹⁻⁵¹ Thus, we were surprised in 2014 when we observed that oxygenation of a Mn^{II} complex supported by a pentadentate, amide-containing ligand in MeCN at room temperature resulted in the formation of a mononuclear Mn^{III} -hydroxo complex in near quantitative yield (see Figure 3).³³ The crystal structure of $[\text{Mn}^{\text{III}}(\text{OH})(\text{dpaq})](\text{OTf})$ revealed no steric bulk around the Mn^{III} -hydroxo unit, and this observation caused us to wonder at the ease of generation of this complex. The solid-state structure did

reveal intermolecular hydrogen-bonding between the hydroxo ligand of one $[\text{Mn}^{\text{III}}(\text{OH})(\text{dpaq})]^+$ cation and the carbonyl oxygen of a second cation, but we presumed that this interaction would not persist in solution. Nonetheless, the half-life of $[\text{Mn}^{\text{III}}(\text{OH})(\text{dpaq})](\text{OTf})$ in MeCN at room temperature was estimated to be 26 days, making this Mn^{III} -hydroxo adduct remarkably stable.³³

In spite of the high thermal stability of $[\text{Mn}^{\text{III}}(\text{OH})(\text{dpaq})](\text{OTf})$, this Mn^{III} -hydroxo species was also capable of oxidizing the O–H and C–H bonds of certain substrates. In an attempt to mimic the reactivity of MnLOX , we explored the ability of $[\text{Mn}^{\text{III}}(\text{OH})(\text{dpaq})](\text{OTf})$ to oxidize the C–H bond of xanthene (Figure 4). The weakest C–H bonds in xanthene are bis-benzylic and have bond dissociation free energies (BDFE) similar to that of the bis-allylic C–H bonds in the unsaturated fatty acid substrate of MnLOX (ca. 73 and 77 kcal mol⁻¹, respectively).^{40, 52} The addition of 250 equiv. xanthene to $[\text{Mn}^{\text{III}}(\text{OH})(\text{dpaq})](\text{OTf})$ in MeCN at 50 °C did cause a disappearance of the electronic absorption features of the Mn^{III} -hydroxo that was faster than the thermal decay; however, the reaction was quite slow, with a pseudo-first-order rate constant (k_{obs}) of $8 \times 10^{-4} \text{ s}^{-1}$.³³ Nonetheless, this report was just the second example of C–H bond oxidation by a synthetic Mn^{III} -hydroxo adduct at the time, the first being C–H bond oxidation by the $[\text{Mn}^{\text{III}}(\text{OH})(\text{PY5})]^{2+}$ (Figure 4).⁴⁸ The k_{obs} for xanthene oxidation by $[\text{Mn}^{\text{III}}(\text{OH})(\text{dpaq})]^+$ is only 10-fold less than that estimated for $[\text{Mn}^{\text{III}}(\text{OH})(\text{PY5})]^{2+}$ under a similar excess of xanthene.⁶ These reactions are presumed to occur by a CPET mechanism. For hydrocarbon oxidation by $[\text{Mn}^{\text{III}}(\text{OH})(\text{PY5})]^{2+}$, H/D KIEs over 1.5 and a reasonably linear log(k_2) versus substrate BDE plot are suggestive of a CPET mechanism. As similar data could not be obtained for $[\text{Mn}^{\text{III}}(\text{OH})(\text{dpaq})]^+$, CPET remains the presumptive mechanism for C–H bond oxidation.

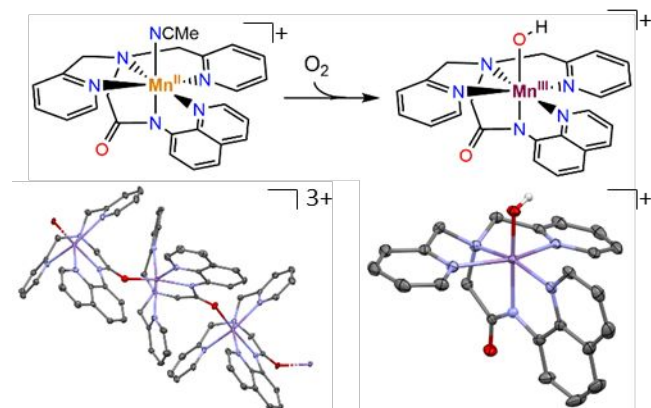


Figure 3. Top: Oxygenation of $[\text{Mn}^{\text{II}}(\text{dpaq})(\text{NCMe})]^+$ in MeCN yields the mononuclear $[\text{Mn}^{\text{III}}(\text{OH})(\text{dpaq})]^+$ complex (dpaq = 2-[bis(pyridin-2-ylmethyl)]amino-N-quinolin-8-yl-acetamidate). Bottom: ORTEP diagrams of X-ray crystal structures of the cationic portion of $[\text{Mn}^{\text{II}}(\text{dpaq})](\text{OTf})$, which is a polymer linked by coordination of the carbonyl oxygen of one $[\text{Mn}^{\text{II}}(\text{dpaq})]^+$ cation to the Mn^{II} center of another cation (left) and cationic portion of $[\text{Mn}^{\text{III}}(\text{OH})(\text{dpaq})](\text{OTf})$ (right). Protons have been omitted from the ORTEP diagrams, with the exception of the hydroxo proton in $[\text{Mn}^{\text{III}}(\text{OH})(\text{dpaq})](\text{OTf})$.

Given the sluggish reactivity of $[\text{Mn}^{\text{III}}(\text{OH})(\text{dpaq})]^+$ towards even activated C–H bonds, we turned to O–H bond oxidation reactions. Hydrogen atoms from O–H bonds are abstracted

more rapidly than from C–H bonds even when the BDFEs are the same.⁵³ In line with this expectation, $[\text{Mn}^{\text{III}}(\text{OH})(\text{dpaq})]^+$ oxidized 2,6-*t*-butyl-4-*X*-phenols ($X = \text{H}, t\text{-Bu}, \text{Me}, \text{and MeO}$) with O–H BDFEs of 74 to 78.5 kcal mol⁻¹.³³ We also explored TEMPOH oxidation by $[\text{Mn}^{\text{III}}(\text{OH})(\text{dpaq})]^+$. Although as a substrate TEMPOH provides no mimicry of the biological reactivity of a Mn^{III}-hydroxo unit, the reaction with TEMPOH is mechanistically informative. The low acidity and quite positive one-electron reduction potential of TEMPOH ($\text{p}K_{\text{a}} = 41$ and $E^{\circ} = 0.71$ V vs. $\text{FeCp}_2^+/\text{FeCp}_2$ in MeCN), along with its small BDFE (66.5 kcal mol⁻¹),⁵² render CPET from TEMPOH considerably more favourable than stepwise electron and proton-transfer processes.⁵² In addition, Kovacs and co-workers had recently described a Mn^{III}-hydroxo complex with a thiolate-containing, monoanionic N₄S ligand capable of TEMPOH oxidation with a remarkably large second-order rate constant (k_2) of 2 100 M⁻¹s⁻¹ (Figure 4). We thus envisioned that examining the rate of TEMPOH oxidation by $[\text{Mn}^{\text{III}}(\text{OH})(\text{dpaq})]^+$ would provide another point of comparison for CPET reactions of Mn^{III}-hydroxo centres.

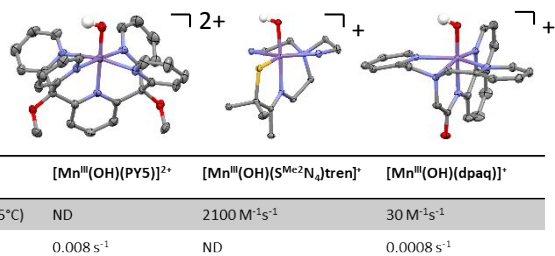


Figure 4. ORTEP diagrams of Mn^{III}-hydroxo complexes (top) and corresponding kinetic data (bottom) for substrate oxidation reactions. With the exception of the hydroxo protons, the ORTEP diagrams do not include hydrogen atoms. The k_2 for TEMPOH oxidation by $[\text{Mn}^{\text{III}}(\text{OH})(\text{dpaq})]^+$ was estimated using the k_2 at -35 °C (1.1 M⁻¹s⁻¹) and published activation parameters from ref. ³¹. The k_{obs} for xanthene oxidation by $[\text{Mn}^{\text{III}}(\text{OH})(\text{PY5})]^{2+}$ was estimated using the published k_{obs} vs. [xanthene] plot in ref. ⁴⁸. Here we have used the k_{obs} for comparison, as the slow rate of reaction of $[\text{Mn}^{\text{III}}(\text{OH})(\text{dpaq})]^+$ with xanthene prevents the determination of a second-order rate constant. The rate constant for $[\text{Mn}^{\text{III}}(\text{OH})(\text{S}^{\text{Me}2}\text{N}_4)\text{tren}]^+$ is from ref. ⁵⁴.

The reaction of TEMPOH with $[\text{Mn}^{\text{III}}(\text{OH})(\text{dpaq})]^+$ proceeds with a k_2 of 1.1 M⁻¹ s⁻¹ at -35 °C in MeCN (Figure 5). (The rate constant was originally reported to be the much smaller value of $1.3(1) \times 10^{-1}$ M⁻¹ s⁻¹.³³ However, the rate was re-evaluated after determining the role of water in the solution chemistry of $[\text{Mn}^{\text{III}}(\text{OH})(\text{dpaq})]^+$; *vide infra*). The rate constant for TEMPOH oxidation by $[\text{Mn}^{\text{III}}(\text{OH})(\text{dpaq})]^+$ can be compared with that of $[\text{Mn}^{\text{III}}(\text{OH})(\text{S}^{\text{Me}2}\text{N}_4)\text{tren}]^+$ when corrections are made for the different reaction temperatures (-35 °C and 25 °C, respectively) using Eyring parameters.³¹ From this comparison, TEMPOH oxidation by $[\text{Mn}^{\text{III}}(\text{OH})(\text{dpaq})]^+$ is ca. 100-fold slower than that of $[\text{Mn}^{\text{III}}(\text{OH})(\text{S}^{\text{Me}2}\text{N}_4)\text{tren}]^+$ (k_2 of ca. 30 and 2 100 M⁻¹s⁻¹ at 25 °C, respectively).⁵⁴ However, the scope of reactivity for $[\text{Mn}^{\text{III}}(\text{OH})(\text{S}^{\text{Me}2}\text{N}_4)\text{tren}]^+$ is more limited, as $[\text{Mn}^{\text{III}}(\text{OH})(\text{S}^{\text{Me}2}\text{N}_4)\text{tren}]^+$ is unable to attack the O–H bonds of phenols,⁵⁴ while $[\text{Mn}^{\text{III}}(\text{OH})(\text{dpaq})]^+$ is capable of phenol oxidation.³³ Thus, $[\text{Mn}^{\text{III}}(\text{OH})(\text{S}^{\text{Me}2}\text{N}_4)\text{tren}]^+$ is kinetically more reactive but thermodynamically more limited. This result is in accord with the BDFEs for the corresponding Mn^{II}-aqua complexes (70.1 kcal mol⁻¹ and 79.4 kcal mol⁻¹ for

$[\text{Mn}^{\text{II}}(\text{OH}_2)(\text{S}^{\text{Me}2}\text{N}_4(\text{tren}))]^+$ and $[\text{Mn}^{\text{II}}(\text{OH}_2)(\text{dpaq})]^+$, respectively).^{54, 55} However, CPET reaction rates are typically enhanced with greater thermodynamic driving force, making the kinetic abilities of $[\text{Mn}^{\text{II}}(\text{OH}_2)(\text{S}^{\text{Me}2}\text{N}_4(\text{tren}))]^+$ impressive.

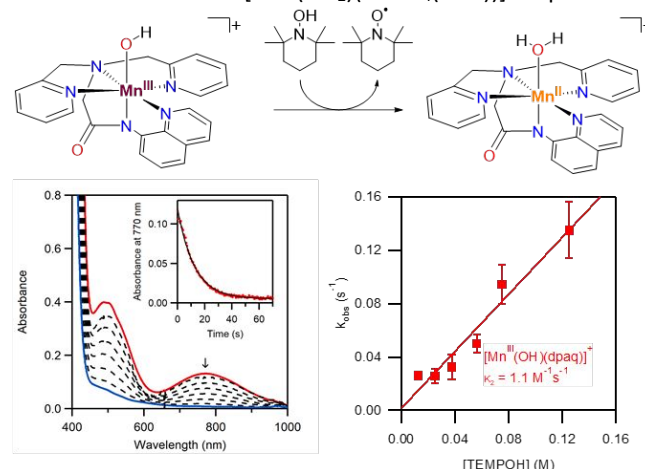


Figure 5. Top: Reaction between $[\text{Mn}^{\text{III}}(\text{OH})(\text{dpaq})]^+$ and TEMPOH. Bottom left: Electronic absorption spectra of a solution of 1.25 mM $[\text{Mn}^{\text{III}}(\text{OH})(\text{dpaq})]^+$ before (red) and after (blue) the addition of 60 eq. TEMPOH. The inset shows the decay of the feature at 770 nm as a function of time. Bottom right: Plot of observed rate constants as a function of TEMPOH concentration at -35 °C.

Equilibrium between mononuclear hydroxomanganese(III) and (μ -oxo)dimanganese(III,III) species.

While pursuing Mn K-edge X-ray absorption studies of $[\text{Mn}^{\text{III}}(\text{OH})(\text{dpaq})](\text{OTf})$,⁵⁶ we collected data for a sample prepared in frozen MeCN. Unexpectedly, we observed a large peak in the Fourier transform (FT) EXAFS spectrum at 3.25 Å (Figure 6).³¹ This prominent peak was absent in corresponding data collected for a solid-state sample of $[\text{Mn}^{\text{III}}(\text{OH})(\text{dpaq})](\text{OTf})$ (powder sample ground in boron nitride; see Figure 6).^{31, 56} This result was the first hint that the solution chemistry of $[\text{Mn}^{\text{III}}(\text{OH})(\text{dpaq})](\text{OTf})$ was more complex than we had presumed.

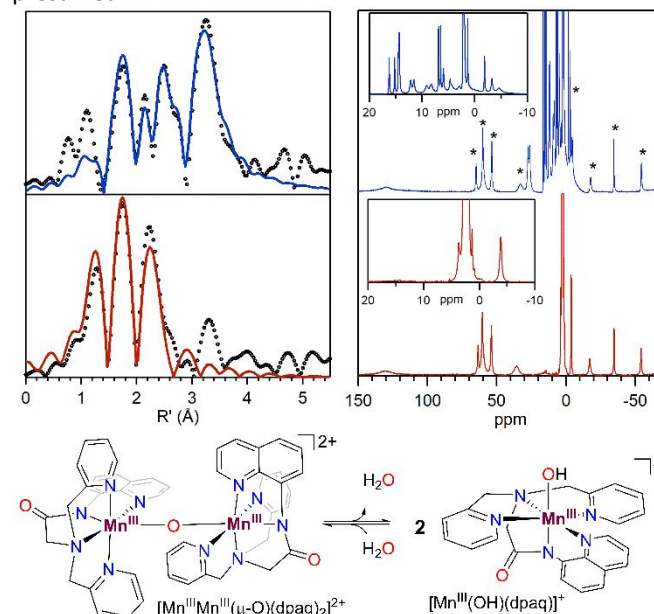


Figure 6. Top-left: Fourier transforms of k^3 -weighted Mn K-edge EXAFS spectra (circles) and fits (lines) for $[\text{Mn}^{\text{III}}(\text{OH})(\text{dpaq})](\text{OTf})$ in dried MeCN (top) and in the solid state

(bottom). Top-right: ^1H NMR spectra of $[\text{Mn}^{\text{III}}(\text{OH})(\text{dpaq})](\text{OTf})$ dissolved in dried d_3 -MeCN (top) and dried d_3 -MeCN with 880 equiv. of D_2O added (bottom). Bottom: Equilibrium reaction of $[\text{Mn}^{\text{III}}\text{Mn}^{\text{III}}(\mu\text{-O})(\text{dpaq})_2]^{2+}$ and $[\text{Mn}^{\text{III}}(\text{OH})(\text{dpaq})]^+$.

The prominent FT EXAFS peak at 3.25 Å for $[\text{Mn}^{\text{III}}(\text{OH})(\text{dpaq})](\text{OTf})$ in MeCN could be well fit with multiple-scattering pathways involving a Mn–O–Mn unit with a Mn...Mn separation of 3.55 Å.³¹ This metal-metal separation is similar to that observed in (μ -oxo)diamanganese(III,III) complexes.^{54, 57} Kovacs⁵⁴ and Mascharak⁵⁷ had previously demonstrated that (μ -oxo)diamanganese(III,III) complexes can form mononuclear Mn^{III}-hydroxo or Mn^{III}-alkoxo products upon reaction with H_2O or alcohols. Our EXAFS data provided circumstantial evidence that dissolution of the $[\text{Mn}^{\text{III}}(\text{OH})(\text{dpaq})](\text{OTf})$ salt in MeCN led to formation of a (μ -oxo)diamanganese(III,III) species, at least at cryogenic temperatures (the XAS data were collected at 10 K). What was needed was a means of probing this potential reaction in solution and at temperatures relevant to our kinetic experiments.

Characterization of Mn^{III}-Schiff base complexes in the 1980s and 1990s benefited from the use of ^1H NMR spectroscopy to distinguish mono- and multinuclear complexes.^{58–60} The ^1H NMR resonances of the mononuclear $S = 2$ Mn^{III} complexes were broad and often shifted outside the range observed for diamagnetic complexes (ca. 14 – 0 ppm). In contrast, antiferromagnetically coupled binuclear species showed sharper signals within the diamagnetic region. We therefore performed ^1H NMR experiments for $[\text{Mn}^{\text{III}}(\text{OH})(\text{dpaq})](\text{OTf})$ in d_3 -MeCN to further understand the solution-phase chemistry of this complex. When the crystalline $[\text{Mn}^{\text{III}}(\text{OH})(\text{dpaq})](\text{OTf})$ salt was dissolved in dried d_3 -MeCN (Figure 6), we observed 28 resonances in the ^1H NMR spectrum from 130 to -60 ppm. Because only 15 inequivalent protons are expected for the $[\text{Mn}^{\text{III}}(\text{OH})(\text{dpaq})]^+$ cation, these data immediately revealed the presence of multiple species in solution at room temperature.

Further insight into the nature of these species was obtained by examining the temperature-dependence of the ^1H NMR resonances. Of the 28 total resonances, nine shifted markedly toward the diamagnetic region and sharpened with increasing temperature. This Curie behaviour^{58, 61, 62} marks these resonances as arising from $[\text{Mn}^{\text{III}}(\text{OH})(\text{dpaq})]^+$, which has a paramagnetic ($S = 2$) ground state. In contrast, many of the remaining resonances displayed anti-Curie behaviour,^{61–63} shifting slightly from the diamagnetic region with increasing temperature. This behaviour is consistent with an antiferromagnetically coupled system with an $S = 0$ ground state. Thermal population of paramagnetic excited states causes the shift of the resonances from the diamagnetic region with increasing temperature. Previous examinations of complexes with (μ -oxo)diamanganese(III,III) cores had revealed strong antiferromagnetic coupling between the Mn^{III} centres, giving $S = 0$ ground states.^{57, 64, 65} Definitive evidence for the assignment of the diamagnetic species observed by ^1H NMR spectroscopy as a (μ -oxo)diamanganese(III,III) species came from studies of derivatives of dpaq, where the 5-quinoline position *para* to the amide nitrogen was substituted with electron-withdrawing (Cl and NO_2) and electron-donating

(OMe) groups. For the $\text{dpaq}^{5\text{Cl}}$ ligand, we used X-ray crystallography to characterize both the $[\text{Mn}^{\text{III}}(\text{OH})(\text{dpaq}^{5\text{Cl}})]^+$ and $[\text{Mn}^{\text{III}}\text{Mn}^{\text{III}}(\mu\text{-oxo})(\text{dpaq}^{5\text{Cl}})_2]^{2+}$ complexes (Figure 7).⁶⁶ The (μ -oxo)diamanganese(III,III) complex showed a linear Mn–O–Mn core (177° bond angle), with Mn–O distances of 1.79 Å and a Mn...Mn separation of 3.58 Å. This structure comports appropriately to that found for $[\text{Mn}^{\text{III}}\text{Mn}^{\text{III}}(\mu\text{-O})(\text{dpaq})_2]^{2+}$ by the analysis of low-temperature EXAFS data.

Given the previous observations that (μ -oxo)diamanganese(III,III) species could be converted to hydroxomanganese(III) adducts upon the addition of water,^{54, 57} we investigated the effect of added water on the ^1H NMR spectrum of $[\text{Mn}^{\text{III}}(\text{OH})(\text{dpaq})](\text{OTf})$ dissolved in dried d_3 -MeCN. The addition of 880 equiv. water to this solution resulted in the complete disappearance of all the ^1H NMR signals associated with the diamagnetic (μ -oxo)diamanganese(III,III) species (Figure 6).³¹ This conversion was complete within ca. 20 minutes at 25 °C. We could now use water to more properly investigate the properties of the Mn^{III}-hydroxo complex. We emphasize that the dissolution of pure crystals of $[\text{Mn}^{\text{III}}(\text{OH})(\text{dpaq})](\text{OTf})$ in dried MeCN will result in the formation of a mixture of $[\text{Mn}^{\text{III}}(\text{OH})(\text{dpaq})]^+$ and $[\text{Mn}^{\text{III}}\text{Mn}^{\text{III}}(\mu\text{-oxo})(\text{dpaq})_2]^{2+}$ species, the precise ratio of which will depend on the amount of trace water present in the MeCN (Figure 6). For example, dissolution of the $[\text{Mn}^{\text{III}}(\text{OH})(\text{dpaq})](\text{OTf})$ salt in MeCN with 64 ± 9 ppm H_2O yields a 20:80 (mol:mol in Mn) ratio of Mn^{III}-hydroxo and (μ -oxo)diamanganese(III,III) species.³¹

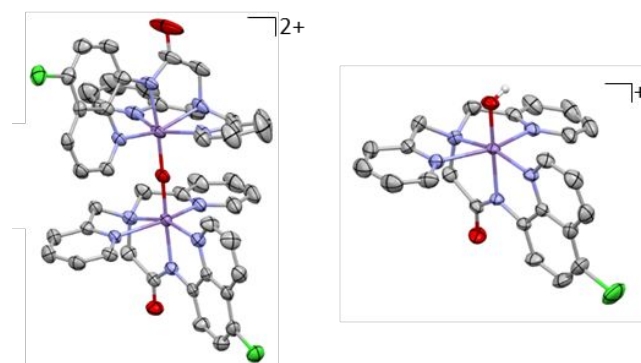


Figure 7. ORTEP diagrams the cationic portions of $[\text{Mn}^{\text{III}}\text{Mn}^{\text{III}}(\mu\text{-oxo})(\text{dpaq}^{5\text{Cl}})_2](\text{OTf})_2$ (left) and $[\text{Mn}^{\text{III}}(\text{OH})(\text{dpaq}^{5\text{Cl}})](\text{OTf})$ (right). Hydrogens have been removed for clarity, with the exception of the hydroxo proton in $[\text{Mn}^{\text{III}}(\text{OH})(\text{dpaq}^{5\text{Cl}})](\text{OTf})$.

Mechanisms of formation of Mn^{III}-hydroxo adducts from Mn^{II} compounds and O_2 .

Once we had a better understanding of the solution chemistry of $[\text{Mn}^{\text{III}}\text{Mn}^{\text{III}}(\mu\text{-O})(\text{dpaq})_2]^{2+}$ and $[\text{Mn}^{\text{III}}(\text{OH})(\text{dpaq})]^+$, we were in a position to determine the mechanism by which these species were formed upon O_2 activation. We were particularly interested in comparing O_2 activation pathways leading to $[\text{Mn}^{\text{III}}(\text{OH})(\text{dpaq})]^+$ and the $[\text{Mn}^{\text{I}}(\text{OH})(\text{dpaq}^{2\text{Me}})]^+$ derivative that contains a methyl substituent adjacent to the hydroxo ligand (Figure 8).³² The steric bulk of this methyl group prevents formation of the $[\text{Mn}^{\text{III}}\text{Mn}^{\text{III}}(\mu\text{-O})(\text{dpaq}^{2\text{Me}})_2]^{2+}$ dimer. ^1H NMR spectra collected for $[\text{Mn}^{\text{III}}(\text{OH})(\text{dpaq}^{2\text{Me}})](\text{OTf})$ dissolved even in dried d_3 -MeCN showed no evidence for the formation of the (μ -oxo)diamanganese(III,III) species.³¹

Dioxygen titration experiments provided strong evidence for differences in O_2 activation pathways leading to $[Mn^{III}(OH)(dpaq)]^+$ and $[Mn^{III}(OH)(dpaq^{2Me})]^+$.⁶⁷ While the addition of 0.25 equiv. O_2 to $[Mn^{II}(dpaq)](OTf)$ was required for maximal formation of $[Mn^{III}(OH)(dpaq)]^+$, the maximal formation of $[Mn^{III}(OH)(dpaq^{2Me})]^+$ from $[Mn^{II}(dpaq^{2Me})](OTf)$ required 0.5 equiv. O_2 (Figure 8). In addition, the oxygenation of $[Mn^{II}(dpaq^{Me})](OTf)$ in d_3 -MeCN resulted in a ca. 50:50 mixture of Mn^{III} -OH and Mn^{III} -OD products, while no deuterated products were observed when $[Mn^{II}(dpaq)](OTf)$ was treated with O_2 in d_3 -MeCN.⁶⁷

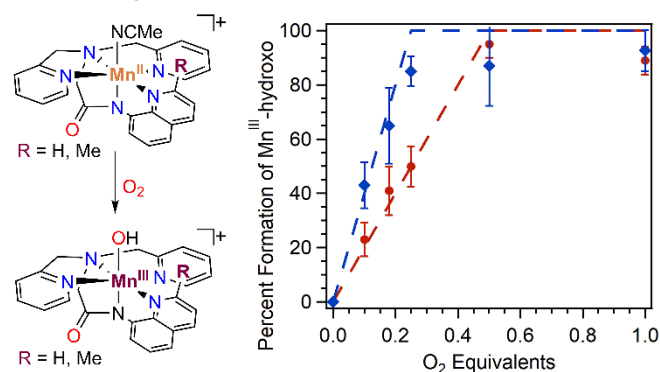


Figure 8. Left: Formation of $[Mn^{III}(OH)(dpaq)]^+$ ($R = H$; blue diamonds) and $[Mn^{III}(OH)(dpaq^{2Me})]^+$ ($R = Me$; red circles) from O_2 activation by their respective solvento complexes. Right: Percent formation of Mn^{III} -hydroxo adducts from their Mn^{II} precursors as a function of equivalents of O_2 . The dashed traces indicated that expected for 0.25:1 (blue) and 0.5:1 (red) O_2 :Mn stoichiometries.

Previous investigations of O_2 activation by Mn^{II} centres have provided a framework for understanding these observations (Figure 9).^{51, 68} In the first step, a mononuclear Mn^{II} centre reacts with O_2 to generate a Mn^{III} -superoxo adduct. This adduct is trapped by a second Mn^{II} centre to form a μ -peroxodimanganese(III,III) species. Kovacs and co-workers have provided evidence for both intermediates.⁶⁸ In their work, oxygenation of a Mn^{II} complex with an anionic N_4S ligand led to the isolation and crystallographic characterization of a *trans*- μ -1,2-peroxodimanganese(III,III) complex.⁶⁸ Stopped-flow kinetic studies provided evidence for the accumulation of a presumed mononuclear superoxomanganese(III) adduct preceding formation of this μ -peroxodimanganese(III,III) complex.⁶⁸

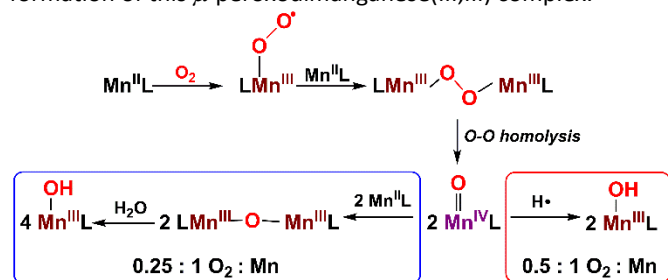


Figure 9. Schematic representation Mn^{III} -hydroxo formation by O_2 activation of Mn^{II} complexes, where L is a generic ligand. The blue and red boxes indicate Mn^{III} -hydroxo formation by dimer-formation and hydrogen-atom transfer pathways, respectively.

The μ -peroxodimanganese(III,III) species is proposed to undergo O–O bond homolysis, giving either two mononuclear Mn^{IV} -oxo adducts (Figure 9) or a bis(μ -oxo)dimanganese(IV,IV) intermediate. At this point, the mechanism diverges. In one

scenario, the Mn^{IV} -oxo species attacks unreacted Mn^{II} starting complex, giving the (μ -oxo)dimanganese(III,III) species (Figure 9). Hydrolysis of this intermediate by water gives the observed mononuclear Mn^{III} -hydroxo product. This pathway has a O_2 : Mn^{II} ratio of 0.25:1 and would not result in any deuterium incorporation from solvent. The observations for O_2 activation by $[Mn^{II}(dpaq)](OTf)$ are most consistent with this pathway.⁶⁷

Alternatively, the Mn^{IV} -oxo intermediate could abstract a hydrogen-atom from solvent, leading to the direct formation of the mononuclear Mn^{III} -hydroxo product (Figure 9). This pathway, which gives a 0.5:1 O_2 : Mn^{II} ratio and leads to Mn^{III} -OD formation when using deuterated solvent, appears to be that followed by $[Mn^{II}(dpaq^{2Me})](OTf)$.⁶⁷ Presumably, the modest steric encumbrance imposed by the 2-Me-quinolinyl group in the $dpaq^{2Me}$ ligand is sufficient to disfavour formation of the (μ -oxo)dimanganese(III,III) species. In support, the other example of a Mn^{III} -hydroxo adduct generated by this hydrogen-atom transfer pathway comes from Borovik and co-workers, who likewise used a sterically encumbered ligand that prevents formation of a (μ -oxo)dimanganese(III,III) intermediate.⁵¹ This pathway for O_2 activation is appealing from a catalyst design standpoint, as one could envision the putative Mn^{IV} -oxo intermediate reacting with a substrate rather than solvent.

Ligand perturbations modulate the thermodynamic and kinetic properties of the Mn^{III} -hydroxo unit.

Comparisons of the reactivity of $[Mn^{III}(OH)(dpaq)]^+$ with the $[Mn^{III}(OH)(PY5)]^{2+}$ and $[Mn^{III}(OH)(S^{Me}N_4(tren))]^+$ complexes (Figure 4) are of limited utility given the small sample size and the large differences in coordination sphere for these complexes. To provide a more meaningful assessment of the relationship between ligand properties and Mn^{III} -hydroxo reactivity, we generated a series of Mn^{III} -hydroxo adducts using derivatives of the $dpaq$ ligand.⁶⁶ We were motivated by Hitomi and co-workers, who had generated a set of manganese-nitrosyl complexes using $dpaq$ derivatives functionalized with electron-withdrawing ($-Cl$ and $-NO_2$) and electron-donating ($-OMe$) groups in the 5-quinolinyl position (Figure 10).⁶⁹ Perturbations in the Mn reduction potential of ca. 150 mV was observed for this Mn-NO series.⁶⁹ We reasoned that the corresponding Mn^{III} -hydroxo complexes could show similar variations in reduction potential, which would influence both the thermodynamics and kinetics for CPET reactions.

Oxidation of each of the $[Mn^{II}(dpaq^{5R})](OTf)$ complexes in MeCN led to the formation of mixtures of $[Mn^{III}Mn^{III}(\mu-O)(dpaq^{5R})_2]^{2+}$ and $[Mn^{III}(OH)(dpaq^{5R})]^+$ species.⁶⁶ These mixtures were identified by 1H NMR spectroscopy, and each of the $[Mn^{III}Mn^{III}(\mu-O)(dpaq^{5R})_2](OTf)$ complexes was structurally characterized by X-ray crystallography. Only in the case of $[Mn^{III}(OH)(dpaq^{5Cl})](OTf)$ did we obtain a crystal structure of the mononuclear Mn^{III} -hydroxo species (Figure 7).⁵⁵ Nonetheless, addition of 880 equiv. water to d_3 -MeCN solutions of the $[Mn^{III}Mn^{III}(\mu-O)(dpaq^{5R})_2]^{2+}$ and $[Mn^{III}(OH)(dpaq^{5R})]^+$ species was sufficient to cause the signals associated with the dimer to disappear and cause the signals associated with the Mn^{III} -hydroxo complex to increase in intensity. Therefore, all analyses

of the properties and reactivity of the $[\text{Mn}^{\text{III}}(\text{OH})(\text{dpaq}^{5\text{R}})]^+$ complexes was performed in a 98:2 MeCN:H₂O mixture, where the Mn^{III}-hydroxo is by far the dominant species in solution.

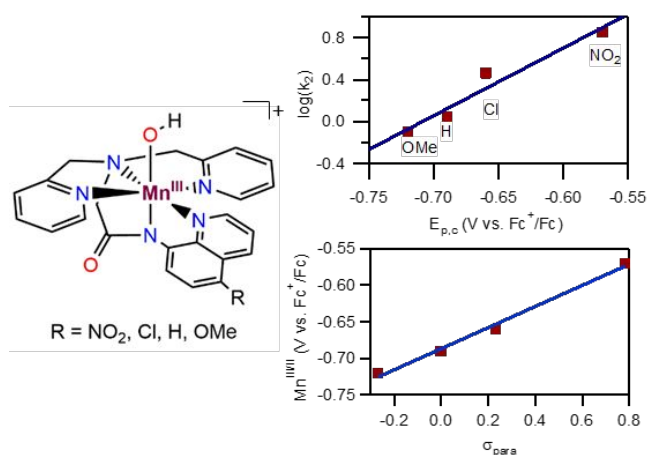


Figure 10. Left: Schematic structure of $[\text{Mn}^{\text{III}}(\text{OH})(\text{dpaq}^{5\text{R}})]^+$ complexes with substituents *para* to the amide nitrogen. Right: Dependence of the reaction rate for TEMPOH oxidation by the $[\text{Mn}^{\text{III}}(\text{OH})(\text{dpaq}^{5\text{R}})]^+$ complexes as a function of the Mn^{III/II} cathodic peak potential, $E_{\text{p,c}}$ (top), and the Mn^{III/II} peak potentials as a function of the σ parameter.

As anticipated, the variations in the donor properties of the supporting $\text{dpaq}^{5\text{-R}}$ ligands led to a systematic shift in the Mn^{III/II} peak potential observed by cyclic voltammetry (Figure 10). The overall shift is modest (less than 200 mV for the extremes of $[\text{Mn}^{\text{III}}(\text{OH})(\text{dpaq}^{5\text{NO}_2})]^+$ and $[\text{Mn}^{\text{III}}(\text{OH})(\text{dpaq}^{5\text{OMe}})]^+$), but the peak potential correlated linearly to the Hammett σ_{para} value associated with the 5-R substituent (Figure 10).⁶⁶

To assess the consequence of this variation in Mn^{III/II} potential on CPET reactivity, we determined second-order rate constants for TEMPOH oxidation by each $[\text{Mn}^{\text{III}}(\text{OH})(\text{dpaq}^{5\text{R}})]^+$ complex at -35 °C. The largest rate constant ($k_2 = 7(1) \text{ M}^{-1} \text{ s}^{-1}$) was observed for the most electron-deficient Mn^{III}-hydroxo adduct, $[\text{Mn}^{\text{III}}(\text{OH})(\text{dpaq}^{5\text{NO}_2})]^+$, while the electron-rich Mn^{III}-hydroxo unit of $[\text{Mn}^{\text{III}}(\text{OH})(\text{dpaq}^{5\text{OMe}})]^+$ showed the smallest rate constant ($k_2 = 0.8(1) \text{ M}^{-1} \text{ s}^{-1}$).⁶⁶ For the series of Mn^{III}-hydroxo complexes, a plot of $\log(k_2)$ for TEMPOH oxidation versus the experimental Mn^{III/II} peak potentials is linear (Figure 10), suggesting that the rate variations arise from changes in the reaction driving force.

However, the Mn^{III/II} potential represents just one component of the driving force for the formation of the O–H bond in the Mn^{II}-aqua product complex. The O–H BDFE is also affected by the pK_a of the Mn^{II}-aqua species (equation 1; $C_{\text{G,sol}}$ is a solvent-dependent constant).

$$\text{BDFE}_{\text{sol}}(\text{O-H}) = 1.37pK_a + 23.06E^0 + C_{\text{G,sol}} \quad (1)$$

Using the experimental O–H BDFE and Mn^{III/II} potential,⁵⁵ the pK_a of $[\text{Mn}^{\text{II}}(\text{OH})_2(\text{dpaq})]^+$ was determined to be 29.3⁶⁶ (the use of an irreversible peak potential rather than a reduction potential has been used in previous analyses,⁵² but this former approach does introduce additional uncertainty). The high basicity of the Mn^{II}-aqua product shows that the driving force for the CPET reactivity of $[\text{Mn}^{\text{III}}(\text{OH})(\text{dpaq})]^+$ comes largely from the basicity of the O–H bond formed in the product. For the

remaining $[\text{Mn}^{\text{II}}(\text{OH})_2(\text{dpaq}^{5\text{R}})]^+$ complexes, the experimental BDFE and pK_a values have yet to be determined. Therefore, we used DFT computations to predict these parameters for Mn^{II}-aqua complexes of the $\text{dpaq}^{5\text{OMe}}$, $\text{dpaq}^{5\text{Cl}}$, and $\text{dpaq}^{5\text{NO}_2}$ ligands, using the experimental pK_a of $[\text{Mn}^{\text{II}}(\text{OH})_2(\text{dpaq})]^+$ as a reference value.⁶⁶ This computational approach accounts for experimental conditions, as these are included in the reference value, and systematic errors in the DFT treatment largely cancel.⁷⁰

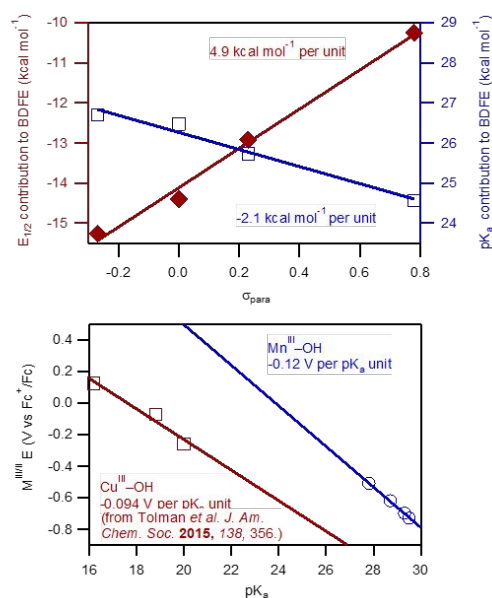


Figure 11. Top: The respective contributions of reduction potential (left axis, red) and pK_a (right axis, blue) to the BDFE of the Mn^{II}-aqua OH bond. Bottom: Reduction potentials as a function of pK_a for the $[\text{Mn}^{\text{III}}(\text{OH})(\text{dpaq}^{5\text{R}})]$ complexes (blue) and for the Cu^{III}-hydroxo complexes (red) described in ref. ⁷¹.

From these computations, the Mn^{III/II} potential and the Mn^{II}-OH₂ pK_a values show an inverse correlation; as the potential becomes more positive, the pK_a decreases.⁶⁶ Consequently, any increase in BDFE caused by an increase in the potential is dampened by a decrease in the pK_a (equation 1). Figure 11 illustrates this trend by plotting the contributions of the DFT-computed pK_a and Mn^{III/II} potentials to the O–H BDFE as a function of the σ_{para} parameter of the 5-quinolinyI substituent. The magnitudes of the slopes observed in these plots illustrate that the opposing effects of the potential and pK_a are unequal, with the potential showing a more pronounced change as a function of σ_{para} . An alternate way to view the potential- pK_a relationship, which was employed by Tolman and co-workers for a series of Cu^{III}-hydroxo complexes,⁷¹ is shown in a plot of the metal(III/II) reduction potential versus the pK_a for the reduced metal(II)-aqua species (Figure 10). In this plot, a slope of -0.059 V per pK_a unit would represent perfect potential- pK_a compensation, where any change in the BDFE caused by a change in the potential would be precisely cancelled by an opposing change in pK_a . For both the Mn^{III}-hydroxo and Cu^{III}-hydroxo complexes, the slopes are more negative than -0.059 V per pK_a and thus the changes in potential are dominant. The reasons for these observations are unclear and worthy of further exploration.

The rate variations observed for the $[\text{Mn}^{\text{III}}(\text{OH})(\text{dpaq})^{\text{5R}}]^+$ complexes highlight the difficulty in achieving large changes in CPET reaction rates through ligand perturbations. One challenge is that the ligand substituents push the potentials and $\text{p}K_{\text{a}}$ terms in equation 1 in opposite directions. An additional challenge is that these ligand perturbations engender only modest changes in the reduction potentials (ca. 150 mV). Even in the absence of any compensating change in the $\text{p}K_{\text{a}}$ (a heuristically useful, albeit unrealistic, scenario), these small changes in the reduction potential would only cause a ca. 3 kcal mol^{-1} change in the O–H BDFE of the Mn^{II} -aqua product. Far more dramatic changes in the metal ion reduction potential, and, consequently, CPET reactivity, can be achieved by modifying the overall charge of the metal complex. For example, Nam and co-workers reported that the Mn^{III} -aqua complex $[\text{Mn}^{\text{III}}(\text{OH}_2)(\text{dpaq})]^{2+}$, which can be formed by reacting $[\text{Mn}^{\text{III}}(\text{OH})(\text{dpaq})]^+$ with triflic acid, has enhanced reactivity towards substrates when compared with $[\text{Mn}^{\text{III}}(\text{OH})(\text{dpaq})]^+$.⁵⁵ This enhancement can be understood primarily through the significantly more positive potential of the Mn^{III} -aqua species than the Mn^{III} -hydroxo adduct (1.03 and -0.10 V vs SCE, respectively). The dramatic rate enhancements observed in this case raise questions. By which mechanism does $[\text{Mn}^{\text{III}}(\text{OH}_2)(\text{dpaq})]^{2+}$ react with substrates? Reactions with phenols proceed with H/D KIEs of 1.7 – 1.8.⁵⁵ If the reaction occurs by CPET or PCET, what is the proton acceptor? Product analysis of the final reaction solution shows the formation of the protonated dpaq-H ligand,⁵⁵ but it is uncertain if this ligand is the initial proton acceptor. Intriguingly, we have recently demonstrated that the $[\text{Mn}^{\text{III}}(\text{OH}_2)(\text{dpaq})]^{2+}$ adduct can also be formed by the reaction of $[\text{Mn}^{\text{III}}(\text{OH})(\text{dpaq})]^+$ with the strong Lewis acids $\text{Sc}(\text{OTf})_3$ and $\text{Al}(\text{OTf})_3$.⁷² These Lewis acids presumably bind to water, a required co-solvent, and greatly increase the Brønsted acidity of the solution, resulting in protonation of the Mn^{III} -hydroxo species.

Mn(IV)-oxo Complexes

The development of synthetic Mn^{IV} -oxo complexes has been inspired in part by the observation of highly reactive Fe^{IV} -oxo intermediates in biological systems.^{8, 14} Early studies of bio-inspired Mn^{IV} -oxo complexes supported by porphyrin and non-porphyrin ligands showed Mn^{IV} -oxo adduct that were only moderately reactive, oxidizing substrates with weak C–H bonds slowly.^{73–78} Thus, Mn^{IV} -oxo adducts were generally considered to be less reactive than their Fe^{IV} -oxo analogues. This assessment changed in 2011, when Nam and co-workers reported that a Mn^{IV} -oxo adduct supported by the neutral, aminopyridyl Bn-TPEN ligand (Figure 12) was capable of attacking the strong C–H bond of cyclohexane.²⁵ This Mn^{IV} -oxo adduct also performed oxygen-atom transfer reactions to thioanisole and its para-substituted derivatives to produce sulfoxides. The basis for the high reactivity of $[\text{Mn}^{\text{IV}}(\text{O})(\text{Bn-TPEN})]^{2+}$ was unclear. While years of research have been dedicated to understanding the grounds for the high reactivity of some Fe^{IV} -oxo complexes,^{79–81} there is far less information concerning corresponding Mn^{IV} -oxo species. Following the initial report of $[\text{Mn}^{\text{IV}}(\text{O})(\text{Bn-TPEN})]^{2+}$,

Nam *et al.*⁸² and our group³⁴ independently described $[\text{Mn}^{\text{IV}}(\text{O})(\text{N4py})]^{2+}$ (Figure 12) as a second example of a reactive Mn^{IV} -oxo adduct supported by a neutral aminopyridyl ligand. Around the same time, Nam, Shaik, and co-workers employed DFT methods to propose a multi-state reactivity model to account for the rapid reactivity of $[\text{Mn}^{\text{IV}}(\text{O})(\text{Bn-TPEN})]^{2+}$ and $[\text{Mn}^{\text{IV}}(\text{O})(\text{N4py})]^{2+}$ in CPET reactions with hydrocarbons.³⁶ As described below, this reactivity model has served as motivation for additional experimental and theoretical studies of $[\text{Mn}^{\text{IV}}(\text{O})(\text{N4py})]^{2+}$ and has provided an outstanding framework for designing new Mn^{IV} -oxo adducts with enhanced reactivity.

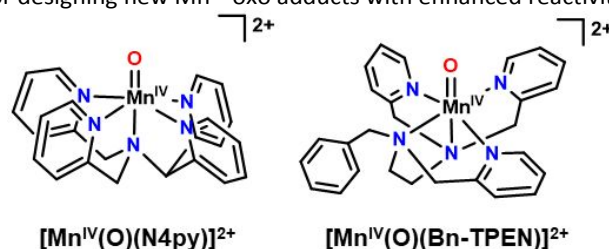


Figure 12. Structures of $[\text{Mn}^{\text{IV}}(\text{O})(\text{N4py})]^{2+}$ and $[\text{Mn}^{\text{IV}}(\text{O})(\text{Bn-TPEN})]^{2+}$ (N4py = *N,N*-bis(2-pyridylmethyl)-*N*-bis(2-pyridyl)methylamine and Bn-TPEN = *N*-benzyl-*N,N',N'*-tris(2-pyridylmethyl)-1,2-diaminoethane).

Experimental and Theoretical Evaluations of the Multi-state Reactivity Model of Mn^{IV} -oxo Complexes.

In the multi-state reactivity model proposed for $[\text{Mn}^{\text{IV}}(\text{O})(\text{N4py})]^{2+}$ and $[\text{Mn}^{\text{IV}}(\text{O})(\text{Bn-TPEN})]^{2+}$, a ligand-field excited state gives rise to a lower energetic barrier for C–H bond oxidation than the ground state (Figure 13, top).^{36, 83} Before the reaction with substrate, the Mn^{IV} -oxo centre has a $^4\text{B}_1$ ground state, with three unpaired electrons in the $\text{b}_2(\text{d}_{xy})$ and $\text{e}(\text{d}_{yz}, \text{d}_{xz})$ orbitals. Along the reaction pathway, the system crosses to the ^4E state, which has a $\text{b}_2(\text{d}_{xy})^1\text{e}(\text{d}_{yz}, \text{d}_{xz})^1\text{b}_1(\text{d}_x^2 - \text{d}_y^2)^1\text{a}_1(\text{d}_z^2)^0$ configuration. The ^4E state is thus related to the $^4\text{B}_1$ ground state by a one-electron excitation from the $\text{e}(\text{d}_{yz}, \text{d}_{xz})$ orbital to the $\text{b}_1(\text{d}_x^2 - \text{d}_y^2)$ orbital. The orbital occupation of the ^4E state places a hole in the low-lying $\text{e}(\text{d}_{yz}, \text{d}_{xz})$ orbital, which is strongly Mn=O π -antibonding. This hole character is presumed to facilitate electron transfer from substrate to the Mn^{IV} centre. In addition, electron transfer on the ^4E surface creates a high-spin ($S = 2$) Mn^{III} product (Figure 13), which should be more stable than the intermediate-spin Mn^{III} product that could be formed on the $^4\text{B}_1$ surface.

Our first step in evaluating this multi-state reactivity model was to determine the energy of the ^4E excited state for $[\text{Mn}^{\text{IV}}(\text{O})(\text{N4py})]^{2+}$. In this endeavour, we took advantage of the unique selection rules of magnetic circular dichroism (MCD) spectroscopy.⁸⁴ The ^4E excited state of $[\text{Mn}^{\text{IV}}(\text{O})(\text{N4py})]^{2+}$ has near orbital degeneracy (near, because the complex does not have a true four-fold rotational axis). Excitation from a non-orbitally-degenerate ground state (such as $^4\text{B}_1$) to a ^4E excited state will appear in the MCD spectrum as a derivative-shaped signal with intensity that increases at lower temperatures. This type of feature, which is called a pseudo-A term, is observed in the MCD spectrum of $[\text{Mn}^{\text{IV}}(\text{O})(\text{N4py})]^{2+}$ at 10 500 cm^{-1} .⁸⁵ This spectral assignment was confirmed using a graphical analysis of the orbitals involved in the electronic transition. Unexpectedly,

the 4E excited-state energy is roughly twice as large as that predicted by DFT computations.⁸⁵ This discrepancy could arise from the unique electronic structure of the 4E state. The initial DFT studies had suggested substantial Mn^{III} -oxyl character in this state;³⁶ this proposal was reinforced by our multireference CASSCF/NEVPT2 computations for $[Mn^{IV}(O)(N4py)]^{2+}$.⁸⁵ However, the CASSCF/NEVPT2 computations also revealed the 4E state to be multiconfigurational, consisting of ca. 15% Mn^{III} -oxyl(π) character at the equilibrium $Mn=O$ bond length of 1.67 Å. This multiconfigurational character increases upon $Mn=O$ bond elongation (which would occur near the CPET transition state). Because of these considerations, it is unclear if DFT is an appropriate theory for treating the electronic structure of Mn^{IV} -oxo complexes in CPET reactions.

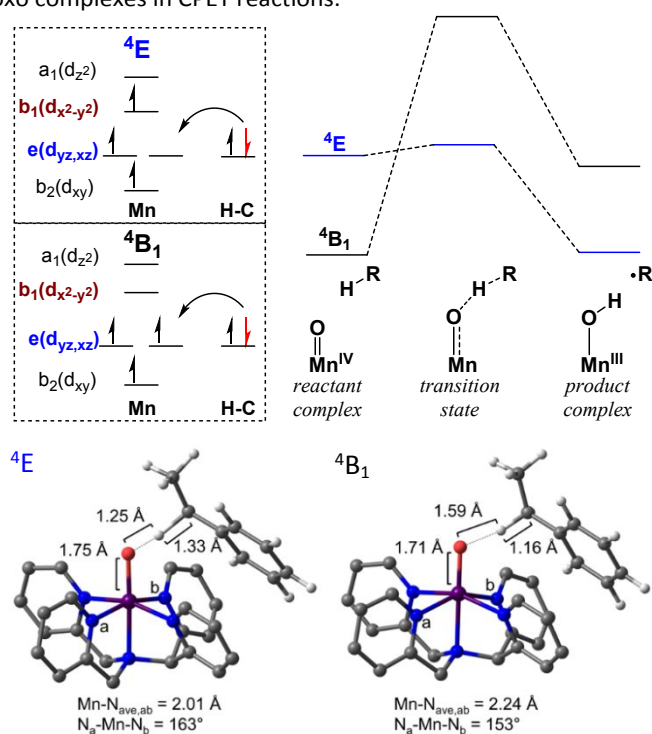


Figure 13. Top left: configurations for the 4E excited state and 4B_1 ground state and possible electron transfer pathway for each state. Top right: simplified reaction coordinate for a CPET reaction involving a Mn^{IV} -oxo and C-H bond containing substrate. Bottom: DFT-optimized 4E (left) and 4B_1 (right) transition-state structures. Adapted with permission from D. B. Rice, A. A. Massie and T. A. Jackson, *Inorg. Chem.*, 2019, **58**, 13902-13916. Copyright 2019 American Chemical Society.

For our second step in evaluating the multi-state reactivity model, we compared experimental activation parameters for ethylbenzene oxidation by $[Mn^{IV}(O)(N4py)]^{2+}$ with computational predictions.⁸⁶ An Eyring analysis of experimental rate constants collected over a range of temperatures gave $\Delta H^\ddagger = 13.5$ kcal mol $^{-1}$ and $T\Delta S^\ddagger = -6.9$ kcal mol $^{-1}$ at 25 ° (Figure 14). DFT methods were used to obtain geometries for reactants, products, and both the 4E and 4B_1 transition states. Each transition state showed a $Mn-O-H(C)$ angle near 115 ° (Figure 13, bottom). This angle implies an interaction between the C-H donor and the Mn^{IV} -oxo $e(d_{yz}, d_{xz})$ MOs that are $Mn=O$ π -antibonding. Such a transition-state interaction represents a π -pathway for CPET. Other than this similarity in the substrate approach angle, the 4B_1 and 4E transition states differ markedly

(Figure 13, bottom). The 4B_1 transition state has pronounced elongations in both the $Mn=O$ and $H-C$ bonds (1.75 and 1.33 Å, respectively at the transition state vs. 1.66 and 1.10 Å for the reactant complex), and the $O\cdots H$ separation is quite short (1.25 Å). Thus, the 4B_1 transition state is late. In contrast, the 4E transition state has shorter $Mn=O$ and $C-H$ bonds of 1.71 and 1.16 Å and a longer $O\cdots H$ separation of 1.59 Å (Figure 13, bottom). The largest change for the 4E transition state relative to the reactant complex is in the $Mn-N_{equatorial}$ bonds, two of which have elongated from 2.01 to 2.24 Å. This elongation serves in part to stabilize the partial occupancy of the $b_1(d_{x^2-y^2})$ MO in the 4E state.

Using these DFT-derived transition-state geometries, we compared the enthalpies of activation using energies from DFT and CASSCF/NEVPT2 computations (Figure 14).⁸⁶ At the DFT level, the activation enthalpy for the 4B_1 transition state is in remarkably good agreement with experiment (13.3 and 13.5 kcal mol $^{-1}$, respectively; see Figure 14). However, the DFT computations predict the 4E transition state to have an even lower ΔH^\ddagger of 3.9 kcal mol $^{-1}$ (Figure 14). The relative ordering of the 4B_1 and 4E transition states is consistent with the previously proposed multi-state reactivity model that predicts a lower barrier on the 4E surface (Figure 13).^{36,87} The unexpectedly small ΔH^\ddagger for the 4E transition state suggests that the DFT energies are subject to some errors. These results also suggest that the agreement between the 4B_1 transition-state energy and the experimental ΔH^\ddagger is coincidental and not necessarily reflective of the involvement of the 4B_1 transition state in the substrate oxidation reaction.

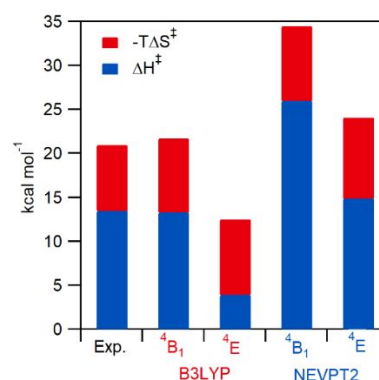


Figure 14. Bar graph showing activation parameters for $[Mn^{IV}(O)(N4py)]^{2+}$ with ethylbenzene from experimental and theoretical methods shown as the summed contributions to ΔG^\ddagger calculated at 25 °C. Reprinted with permission from D. B. Rice, A. A. Massie and T. A. Jackson, *Inorg. Chem.*, 2019, **58**, 13902-13916. Copyright 2019 American Chemical Society.

When the activation enthalpies are instead calculated using single-point energies from CASSCF/NEVPT2 computations, the ΔH^\ddagger for both the 4B_1 and 4E transition states increase by ca. 12 kcal mol $^{-1}$ (Figure 14). This change causes the ΔH^\ddagger parameter for the 4E transition state to be in excellent agreement with experiment (12.2 and 13.5 kcal mol $^{-1}$, respectively). The CASSCF/NEVPT2 ΔH^\ddagger value for the 4B_1 state is in poor agreement with the experimental barrier, being ca. 13 kcal mol $^{-1}$ larger than expected (Figure 14). Thus, the CASSCF/NEVPT2 results appear to provide support for the involvement of the 4E transition

state. It is important to note that both the DFT and CASSCF/NEVPT2 results are in agreement regarding the relative order of the 4E and 4B_1 transition states, but only the multireference method provides quantitative agreement with the experimental activation enthalpy.⁸⁶

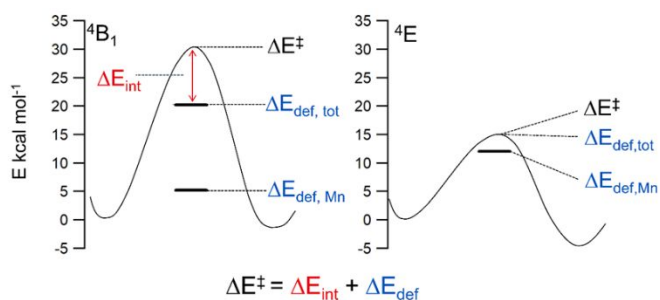


Figure 15. Components contributing to the CASSCF/NEVPT2 activation energy barrier for $[Mn^{IV}(O)(N4py)]^{2+}$ with ethylbenzene for the 4B_1 (left) and 4E_1 (right) states. Reprinted with permission from D. B. Rice, A. A. Massie and T. A. Jackson, *Inorg. Chem.*, 2019, **58**, 13902-13916. Copyright 2019 American Chemical Society.

The promising CASSCF/NEVPT2 results motivated us to investigate contributions to the calculated energy barrier, ΔE^\ddagger , for the 4B_1 and 4E transition states. In this approach,⁸⁸ ΔE^\ddagger is deconstructed into i) a distortion energy (ΔE_{def}), describing the cost of taking the reactants to their transition-state geometries in the absence of any interaction between the reactants; and ii) an interaction energy (ΔE_{int}), encompassing both steric penalties and electronic stabilization that occur when the distorted molecules are brought together at their transition-state separations. Separate distortion energies can be determined for the $[Mn^{IV}(O)(N4py)]^{2+}$ complex and ethylbenzene.

The 4B_1 transition state shows a small distortion energy for the Mn^{IV} -oxo complex ($\Delta E_{def, Mn} \approx +5$ kcal mol⁻¹) but the total ΔE_{def} term is large (Figure 15). The large ΔE_{def} parameter is likely a consequence of the lateness of the transition state (*i.e.*, there is significant C–H bond elongation; see Figure 13). The ΔE_{def} term alone represents ca. +20 kcal mol⁻¹ of the energy barrier. The 4B_1 barrier is also subject to a substantial interaction energy of +10 kcal mol⁻¹. An analysis of the CASSCF bonding description for the 4B_1 transition state showed more localized interactions, consistent with small electronic stabilization, and a mixing of the Mn-based $b_2(d_{xy})$ and $e(d_{yz}, d_{xz})$ MOs.⁸⁶ In several ways, the transition-state electronic structure resembled that observed for π -type CPET on the $S = 1$ surface for Fe^{IV} -oxo complexes.⁸⁹

For the 4E transition state, distortion of the Mn^{IV} -oxo complex is the dominant contributor to the energy barrier ($\Delta E_{def, Mn} \approx +12$ kcal mol⁻¹), but all additional terms are minor. The large $\Delta E_{def, Mn}$ term is consistent with the dramatic changes in $Mn-N_{equatorial}$ distances in the transition state (Figure 13) that prepare the $Mn=O$ unit for interactions with substrate. Because the 4E transition state is early with respect to C–H bond cleavage, substrate distortion is minimal (hence $\Delta E_{def, Mn}$ is nearly equal to $\Delta E_{def, tot}$; see Figure 15). Remarkably, the ΔE_{int} term for the 4E transition state is essentially negligible. The long $O\cdots H$ separation in the 4E transition state (Figure 13) causes reduced steric penalties. In addition, the electronic structure of the 4E transition state, which consists of oppositely-signed spin

density on the Mn and O centres, maximizes overlap between the $Mn=O$ π -antibonding $e(d_{yz}, d_{xz})$ MO and the σ_{CH} orbital of the substrate. This overlap gives rise to highly delocalized transition-state bonding that facilitates the formation of the O–H bond and the cleavage of the C–H bond.⁸⁶

Computational analyses of the multi-state reactivity model of Mn^{IV} -oxo centers have assumed that the 4E transition state is reached thermally rather than photochemically.^{36, 83, 86} This assumption is consistent with the experimental observation that the rates of ethylbenzene and DHA oxidation by $[Mn^{IV}(O)(N4py)]^{2+}$ increase with increasing temperature.^{34, 86} In addition, DFT computations indicate that the 4B_1 and 4E states cross early in the reaction coordinate (ca. 7 kcal mol⁻¹ above the 4B_1 ground state) and before the transition states on either surface.⁸⁶ This crossing allows for thermal population of the 4E surface from the 4B_1 ground state along the reaction coordinate. While we take these lines of evidence to support a thermal state crossing, photophysical studies are warranted to explore whether reactions on the 4E surface can also be accessed photochemically.

Equatorial ligand perturbations modulate the electronic properties and reactivity of Mn^{IV} -oxo adducts.

The multi-state reactivity model for Mn^{IV} -oxo adducts suggests that the barrier for C–H bond oxidation can be reduced by lowering the energy of the 4E excited state (Figure 13). As this excited state derives from an $e(d_{yz}, d_{xz})$ to $b_1(d_x^2 - y^2)$ one-electron excitation, stabilization of the $b_1(d_x^2 - y^2)$ MO should lower the 4E excited-state energy, potentially enhancing the CPET reaction rate. In collaboration with Nordlander and co-workers, we examined this prediction by generating new Mn^{IV} -oxo adducts with N4py derivatives that perturb the equatorial ligand field (Figure 16, top).³⁵ The ^{DM}MN4py ligand features methyl and methoxy groups on two of the pyridyl rings, which increase electron donation to the metal centre in the equatorial plane. The bulky quinolinyl rings of the 2pyN2Q ligand give rise to longer Mn–N bonds and a weaker equatorial ligand field. Formation of the Mn^{IV} -oxo adducts of these ligands was achieved by oxidation of $[Mn^{II}(OTf)(^{DM}MN4py)](OTf)$ and $[Mn^{II}(OH_2)(2pyN2Q)](OTf)_2$ with the oxygen-atom transfer agent iodosylbenzene in CF_3CH_2OH . The electronic absorption spectra of these complexes show characteristic shifts in the near-IR absorption band (Figure 16), which reflect perturbations in the energy of the 4E excited state. As predicted based on the ligand modifications, $[Mn^{IV}(O)(^{DM}MN4py)]^{2+}$ shows the highest-energy 4E excited state, while the 4E excited state of $[Mn^{IV}(O)(2pyN2Q)]^{2+}$ is the lowest in energy for this series (2 400 cm⁻¹ below that of $[Mn^{IV}(O)(^{DM}MN4py)]^{2+}$).³⁵

Geometric structures for these complexes from DFT computations revealed an elongation in the average $Mn-N_{equatorial}$ distance from 1.998 Å for $[Mn^{IV}(O)(^{DM}MN4py)]^{2+}$ to 2.032 Å for $[Mn^{IV}(O)(2pyN2Q)]^{2+}$.^{35, 90} The $[Mn^{IV}(O)(N4py)]^{2+}$ complex had an intermediate $Mn-N_{equatorial}$ distance of 2.001 Å. The computations also revealed that the elongations in the $Mn-N_{equatorial}$ distance leads to a stabilization of the Mn^{IV} $b_1(d_x^2 - y^2)$ MO, and thus the 4E excited state. Unexpectedly, the DFT-

derived structure of $[\text{Mn}^{\text{IV}}(\text{O})(2\text{pyN}2\text{Q})]^{2+}$ showed a tilt in the Mn=O bond.³⁵ This tilt is reflected by an $N_{\text{axial}}\text{--Mn--O}$ axial bond angle of 170.6° . The corresponding angles for $[\text{Mn}^{\text{IV}}(\text{O})(^{\text{DMM}}\text{N}4\text{py})]^{2+}$ and $[\text{Mn}^{\text{IV}}(\text{O})(\text{N}4\text{py})]^{2+}$ are 180° . The tilting of the Mn=O bond for $[\text{Mn}^{\text{IV}}(\text{O})(2\text{pyN}2\text{Q})]^{2+}$ arises because of steric clash between the bulky quinolinyl groups and the oxo binding pocket. A metal-oxo tilt was subsequently observed experimentally in the X-ray crystal structure of $[\text{Fe}^{\text{IV}}(\text{O})(2\text{pyN}2\text{Q})]^{2+}$ ($N_{\text{axial}}\text{--Fe--O}$ bond angle of 170.5°).⁹¹

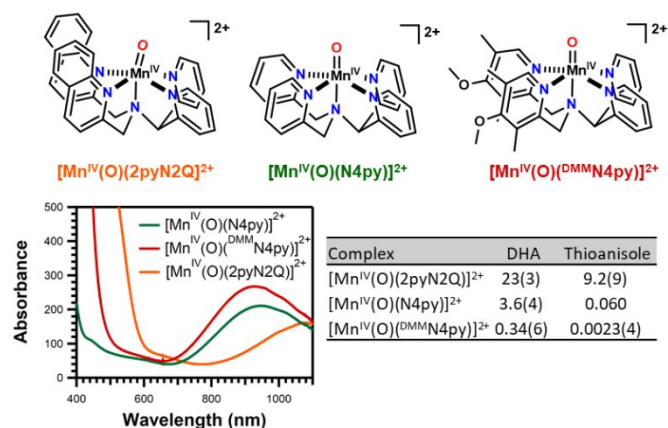


Figure 16. Top: Schematic structures of $[\text{Mn}^{\text{IV}}(\text{O})(2\text{pyN}2\text{Q})]^{2+}$, $[\text{Mn}^{\text{IV}}(\text{O})(\text{N}4\text{py})]^{2+}$, and $[\text{Mn}^{\text{IV}}(\text{O})(^{\text{DMM}}\text{N}4\text{py})]^{2+}$. Bottom-left: Electronic absorption spectra for Mn^{IV}-oxo complexes. Bottom-right: Second-order rate constants (k_2 in $\text{M}^{-1}\text{s}^{-1}$) for the reactions of 9,10-dihydroanthracene (DHA) and thioanisole with the Mn^{IV}-oxo complexes.

Having established the perturbation of the ⁴E excited-state energy through ligand modifications, we assessed the consequence of this perturbation on the ability of the Mn^{IV}-oxo complexes to oxidize hydrocarbons. Second-order rate constants (k_2) were determined for the reaction of each Mn^{IV}-oxo complex with a range of substrates at 25°C ,³⁵ this discussion will focus on 9,10-dihydroanthracene (DHA) as a representative example. The $[\text{Mn}^{\text{IV}}(\text{O})(2\text{pyN}2\text{Q})]^{2+}$ complex showed the largest k_2 of $23(3) \text{ M}^{-1}\text{s}^{-1}$ (Figure 16). This rate constant is 6.4-fold larger than that of $[\text{Mn}^{\text{IV}}(\text{O})(\text{N}4\text{py})]^{2+}$ ($k_2 = 3.6(4) \text{ M}^{-1}\text{s}^{-1}$) and 68-fold larger than that of $[\text{Mn}^{\text{IV}}(\text{O})(^{\text{DMM}}\text{N}4\text{py})]^{2+}$ ($k_2 = 0.34(6) \text{ M}^{-1}\text{s}^{-1}$). This relative rate ordering holds regardless of the hydrocarbon substrate considered.³⁵ The rate trend follows that expected based on the multi-state reactivity model, with a lower ⁴E excited-state energy correlating with a faster reaction rate. The experimental data also suggest that hydrocarbon oxidation is initiated by a CPET step. Specifically, large H/D KIEs of 5.3–11.2 are observed for DHA oxidation by each Mn^{IV}-oxo complex, and plots of $\log(k_2)$ versus substrate BDE for each complex yield a linear relationship.³⁵

Because this multi-state reactivity model was also proposed to be operative in oxygen-atom transfer reactions,⁸⁷ we obtained and compared k_2 values for thioanisole oxidation by these Mn^{IV}-oxo complexes. For this reaction, $[\text{Mn}^{\text{IV}}(\text{O})(2\text{pyN}2\text{Q})]^{2+}$ retained its ranking as fastest oxidant, but the rate enhancement compared to $[\text{Mn}^{\text{IV}}(\text{O})(\text{N}4\text{py})]^{2+}$ and $[\text{Mn}^{\text{IV}}(\text{O})(^{\text{DMM}}\text{N}4\text{py})]^{2+}$ was far more dramatic (Figure 16). In particular, the k_2 for thioanisole oxidation by

$[\text{Mn}^{\text{IV}}(\text{O})(2\text{pyN}2\text{Q})]^{2+}$ was 150- and 4000-fold larger than those of $[\text{Mn}^{\text{IV}}(\text{O})(\text{N}4\text{py})]^{2+}$ and $[\text{Mn}^{\text{IV}}(\text{O})(^{\text{DMM}}\text{N}4\text{py})]^{2+}$, respectively.³⁵

While the comparison of the $[\text{Mn}^{\text{IV}}(\text{O})(\text{N}4\text{py})]^{2+}$, $[\text{Mn}^{\text{IV}}(\text{O})(^{\text{DMM}}\text{N}4\text{py})]^{2+}$, and $[\text{Mn}^{\text{IV}}(\text{O})(2\text{pyN}2\text{Q})]^{2+}$ complexes provides compelling evidence that the equatorial ligand-field strength has a dramatic effect on Mn^{IV}-oxo reactivity, the basis for this relationship is not as clear cut as it might seem. Although the ⁴E excited-state energy shows a correlation with the observed reactivity trends, the Mn^{IV/III} peak potential, observed by cyclic voltammetry, is also strongly correlated with the observed rate constants (Figure 17).³⁵ The latter correlation can be understood based on a standard linear-free energy relationship, where a larger reaction driving force gives rise to a faster reaction rate. A complication in understanding the basis for these various correlations is the small sample size of the complexes considered.

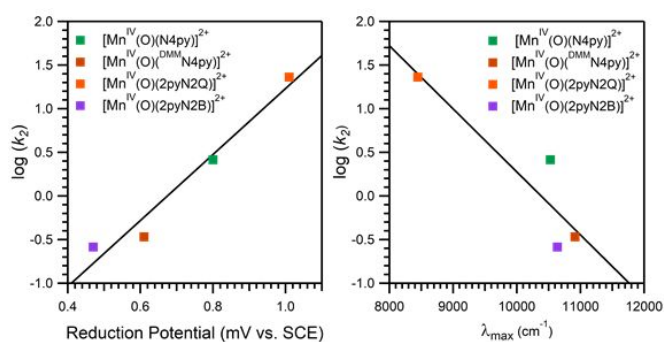


Figure 17. Experimental $\log(k_2)$ values for DHA oxidation by Mn^{IV}-oxo complexes versus Mn^{IV/III} reduction potential (left) and versus the near-infrared electronic absorption band maxima (λ_{max} , which corresponds to the ⁴E excited-state energy) (right).

Advances in the field of Fe^{IV}-oxo chemistry inspired our next choice of ligand derivative. Nordlander and co-workers reported a Fe^{IV}-oxo complex supported by a bis(benzimidazolyl)-containing ligand (2pyN2B).⁹² The rate of reaction by which this complex attacks hydrocarbons was later shown to be similar to that of $[\text{Fe}^{\text{IV}}(\text{O})(2\text{pyN}2\text{Q})]^{2+}$.⁹¹ In collaboration with Nordlander and co-workers, we generated the $[\text{Mn}^{\text{IV}}(\text{O})(2\text{pyN}2\text{B})]^{2+}$ complex (Figure 18) and were surprised by its sluggish reactivity in both CPET reactions with hydrocarbons and oxygen-atom transfer reactions with thioanisole.⁹³ For example, $[\text{Mn}^{\text{IV}}(\text{O})(2\text{pyN}2\text{B})]^{2+}$ shows a k_2 for DHA oxidation that is slightly less than that of $[\text{Mn}^{\text{IV}}(\text{O})(^{\text{DMM}}\text{N}4\text{py})]^{2+}$ ($k_2 = 0.27(2)$ and $0.35(6) \text{ M}^{-1}\text{s}^{-1}$, respectively). For thioanisole oxidation, $[\text{Mn}^{\text{IV}}(\text{O})(2\text{pyN}2\text{B})]^{2+}$ shows an intermediate rate, closest to that of $[\text{Mn}^{\text{IV}}(\text{O})(\text{N}4\text{py})]^{2+}$ ($k_2 = 0.028(3)$ and $0.060(3) \text{ M}^{-1}\text{s}^{-1}$, respectively). The ordering of reactivity leads to the unexpected result that, relatively speaking, $[\text{Mn}^{\text{IV}}(\text{O})(2\text{pyN}2\text{B})]^{2+}$ is a sluggish oxidant, while $[\text{Fe}^{\text{IV}}(\text{O})(2\text{pyN}2\text{B})]^{2+}$ is quite reactive. Understanding the basis for this difference could provide unique insights into CPET reactions of metal-oxo species.

To date, information concerning the metric parameters for the Mn^{IV}-oxo complexes described here have come entirely from Mn K-edge X-ray absorption spectroscopy.^{34, 82, 90} Analysis of Mn K-edge extended X-ray absorption fine structure (EXAFS) data for $[\text{Mn}^{\text{IV}}(\text{O})(\text{N}4\text{py})]^{2+}$, $[\text{Mn}^{\text{IV}}(\text{O})(^{\text{DMM}}\text{N}4\text{py})]^{2+}$, and

$[\text{Mn}^{\text{IV}}(\text{O})(2\text{pyN2B})]^{2+}$ have revealed Mn=O distances of 1.69 - 1.72 Å,^{34, 82, 90} which are in agreement with distances for Mn^{IV} -oxo adducts in similar coordination environments (1.58 - 1.71 Å).^{25, 94} Unexpectedly, the EXAFS distances for $[\text{Mn}^{\text{IV}}(\text{O})(\text{N4py})]^{2+}$, $[\text{Mn}^{\text{IV}}(\text{O})(\text{DMMN4py})]^{2+}$, and $[\text{Mn}^{\text{IV}}(\text{O})(2\text{pyN2B})]^{2+}$ are each 0.04 Å longer than those predicted by DFT computations.⁹⁰ As DFT generally predicts short metal-ligand bond distances with high accuracy, we evaluated the possibility that hydrogen-bonding between the Mn^{IV} -oxo unit and $\text{CF}_3\text{CH}_2\text{OH}$ could cause an elongation in the Mn=O bond length. The DFT-derived structure of $[\text{Mn}^{\text{IV}}(\text{O})(2\text{pyN2B})]^{2+}$ optimized in the presence of two $\text{CF}_3\text{CH}_2\text{OH}$ molecules is shown in Figure 18, right. The consideration of two explicit $\text{CF}_3\text{CH}_2\text{OH}$ molecules during DFT optimization led to the formation of strong oxo- HOCH_2CF_3 hydrogen-bonds. The oxo- HOCH_2CF_3 distances range from 1.62 - 1.75 Å, which indicate strong hydrogen-bonds. These hydrogen-bonds lead to longer Mn=O distances that are in far better agreement with the EXAFS values.⁹⁰ Thus, $\text{CF}_3\text{CH}_2\text{OH}$ might serve a stabilizing role via hydrogen-bonding. Similar computations with $[\text{Fe}^{\text{IV}}(\text{O})(\text{N4py})]^{2+}$ and explicit $\text{CF}_3\text{CH}_2\text{OH}$ molecules lead to weaker oxo- HOCH_2CF_3 hydrogen-bonding interactions (O...H distances 0.1 Å longer than observed for $[\text{Mn}^{\text{IV}}(\text{O})(\text{N4py})]^{2+}$). This change in propensity for hydrogen-bonding could reflect innate differences in basicity for Fe^{IV} -oxo and Mn^{IV} -oxo units.

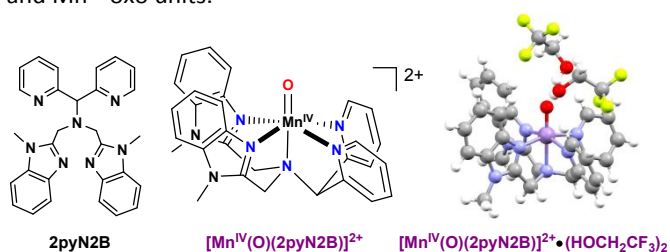


Figure 18. Schematic structures of 2pyN2B ligand (left) and $[\text{Mn}^{\text{IV}}(\text{O})(2\text{pyN2B})]^{2+}$ complex (center). DFT-structure of $[\text{Mn}^{\text{IV}}(\text{O})(2\text{pyN2B})]^{2+}$ in the presence of two HOCH_2CF_3 molecules that hydrogen-bond with the oxo ligand (right).

Perturbations in the Reactivity of Mn^{IV} -oxo Centres by Brønsted and Lewis Acids

Pertinent to our discussion of geometric and electronic structure contributions to the reactivity of $[\text{Mn}^{\text{IV}}(\text{O})(\text{N4py})]^{2+}$ are a series of studies by Nam, Fukuzumi, and co-workers evaluating the influence of strong protic and Lewis acids on the oxidizing abilities of this Mn^{IV} -oxo centre.^{82, 95-97} The addition of these acids to $[\text{Mn}^{\text{IV}}(\text{O})(\text{N4py})]^{2+}$ greatly perturbs the spectroscopic properties of this complex.^{82, 95} Analyses of Mn K-edge EXAFS data for $[\text{Mn}^{\text{IV}}(\text{O})(\text{N4py})]^{2+}$ in the presence of $\text{Sc}^{\text{III}}(\text{OTf})_3$ and triflic acid (HOTf) revealed elongation of the Mn-oxo bond length, consistent with an interaction of these acids with the oxo ligand.^{82, 95} An additional influence of these acids is to shift the $\text{Mn}^{\text{IV/III}}$ potential of $[\text{Mn}^{\text{IV}}(\text{O})(\text{N4py})]^{2+}$ to more positive values (by +0.62 and +0.85 V for $\text{Sc}^{\text{III}}(\text{OTf})_3$ and HOTf, respectively).^{95, 98} This increased oxidizing power causes the acid adducts of $[\text{Mn}^{\text{IV}}(\text{O})(\text{N4py})]^{2+}$ to favour substrate attack by an outer-sphere electron-transfer mechanism.⁹⁹⁻¹⁰¹ For example, $[\text{Mn}^{\text{IV}}(\text{O})(\text{N4py})]^{2+}$ reacts with thioanisole by a

concerted oxygen-atom transfer mechanism, but, when in the presence of $\text{Sc}^{\text{III}}(\text{OTf})_3$ or HOTf, $[\text{Mn}^{\text{IV}}(\text{O})(\text{N4py})]^{2+}$ oxidizes thioanisole by an electron transfer step.⁹⁶ Similar observations have been made for $[\text{Mn}^{\text{IV}}(\text{O})(\text{Bn-TPEN})]^{2+}$.^{97, 98} The $\text{Sc}^{\text{III}}(\text{OTf})_3$ adduct of $[\text{Mn}^{\text{IV}}(\text{O})(\text{Bn-TPEN})]^{2+}$ is also photoactive, performing benzene hydroxylation upon laser irradiation.¹⁰² Transient absorption studies indicate initial population of the ^4E excited state (Figure 13), followed by intersystem crossing to a lower-energy ^2E excited state. The excited-state lifetimes are enhanced by the presence of the Sc^{III} ion.¹⁰² While there are no reports of weaker Lewis acids effecting $[\text{Mn}^{\text{IV}}(\text{O})(\text{N4py})]^{2+}$ and $[\text{Mn}^{\text{IV}}(\text{O})(\text{Bn-TPEN})]^{2+}$, adducts of $[\text{Mn}^{\text{IV}}(\text{O})(\text{dpaq})]^+$ have been reported that employ Lewis acids of varied strength (from Sc^{III} to Ca^{II}).^{103, 104} It is unclear why Mn^{IV} -oxo complexes display different interactions with Lewis acids, although the basicity of the oxo ligand might play a role. The lower net charge of $[\text{Mn}^{\text{IV}}(\text{O})(\text{dpaq})]^+$ as compared to $[\text{Mn}^{\text{IV}}(\text{O})(\text{N4py})]^{2+}$ could support a more basic oxo ligand in the former complex, which could promote interactions even with weak Lewis acids.

Lewis acids have also been used by several researchers to modulate properties and chemical reactivity of Mn^{V} -oxo complexes, but the results here have been more varied. Some Mn^{V} -oxo systems undergo a change in valence state from Mn^{V} -oxo to Mn^{IV} -oxo-ligand-radical upon Lewis-acid binding.¹⁰⁵⁻¹⁰⁷ For these particular adducts, hydrocarbon oxidation still proceeds by a CPET mechanism, but enhancements and de-enhancements relative to the parent Mn^{V} -oxo adduct have been observed.¹⁰⁵⁻¹¹⁰ In other cases, such as the $\text{Sc}^{\text{III}}(\text{OTf})_3$ adduct of $[\text{Mn}^{\text{V}}(\text{O})(\text{TAML})]^-$ (where TAML is a tetramido macrocyclic ligand),¹¹¹ the Mn^{V} oxidation state is retained upon Lewis acid binding. The $[\text{Mn}^{\text{V}}(\text{O})(\text{TAML})]^-:\text{Sc}^{\text{III}}$ complex exhibited enhanced reactivity in oxygen atom and electron transfer reactions when compared to $[\text{Mn}^{\text{V}}(\text{O})(\text{TAML})]^-$, which is in keeping with the more positive one-electron reduction potential of the former complex. Reactivity enhancements for hydrocarbon oxidation were alternately achieved by one-electron oxidation of $[\text{Mn}^{\text{V}}(\text{O})(\text{TAML})]^-$.¹¹² Detailed spectroscopic studies provided strong evidence that the locus of oxidation is the TAML ligand; *i.e.*, the Mn^{V} oxidation state is retained in the oxidized form.

Comparison of Isostructural Mn^{IV} -oxo and Fe^{IV} -oxo Adducts

A unique feature of $[\text{Mn}^{\text{IV}}(\text{O})(\text{N4py})]^{2+}$ and its family of derivatives (Figures 16 and 18) is that the analogous Fe^{IV} -oxo complexes have been reported for each of these ligands.^{91, 92, 113, 114} This collection of complexes provides a basis for comparing the properties of Mn^{IV} -oxo and Fe^{IV} -oxo adducts at parity of ligand sphere and offers insight into how ligand field perturbations affect Mn and Fe centers in different fashions. Such comparisons of the role of the metal identity in oxygen-atom and hydrogen-atom transfer reactions are surprisingly uncommon.^{87, 115-118} The majority of the Fe^{IV} -oxo analogues have been characterized by X-ray crystallography,^{91, 119} while Mn K-edge X-ray absorption spectroscopy has been required for structural characterization of the Mn^{IV} -oxo complexes. It is

curious that, to date, only one Mn^{IV}-oxo species has been characterized by X-ray crystallography.¹²⁰

With regard to chemical reactivity, the most glaring difference between the Mn^{IV}-oxo and Fe^{IV}-oxo analogues is that the latter show far faster rates for oxygen-atom transfer reactions. As a representative example, [Fe^{IV}(O)(2pyN2Q)]²⁺ reacts with thioanisole with a second-order rate constant of 7.4 M⁻¹s⁻¹ at -40 °C,⁹¹ while the corresponding rate for thioanisole oxidation by [Mn^{IV}(O)(2pyN2Q)]²⁺ is 9.2 M⁻¹s⁻¹ at 25 °C.³⁵ The rate constants are comparable in spite of the 65 degree difference in temperature. A more even comparison is provided by thioanisole oxidation by [Fe^{IV}(O)(N4py)]²⁺ and [Mn^{IV}(O)(N4py)]²⁺ in CF₃CH₂OH:CH₃CN (19:1 vol/vol) at 0 °C, where the Fe^{IV}-oxo adduct had a *k*₂ 120-fold larger than the Mn^{IV}-oxo analogue.⁸⁷

Comparisons of the reactivity of Mn^{IV}-oxo and Fe^{IV}-oxo adducts towards hydrocarbons requires qualifications. In each case, these reactions occur by CPET and large H/D kinetic isotope effects have been observed.^{25, 34, 35, 87, 91, 121, 122} Selecting [Fe^{IV}(O)(2pyN2Q)]²⁺ and [Mn^{IV}(O)(2pyN2Q)]²⁺ again as representative examples, the former species is more rapid in cyclohexane oxidation, but only by a factor of 3.5 (*k*₂ of 2.9 × 10⁻² and 8.2 × 10⁻³ M⁻¹s⁻¹ for [Fe^{IV}(O)(2pyN2Q)]²⁺ and [Mn^{IV}(O)(2pyN2Q)]²⁺, respectively; see Figure 19).^{26, 91} In this case, both reactions were at 25 °C. Comparisons of [Fe^{IV}(O)(N4py)]²⁺ and [Mn^{IV}(O)(N4py)]²⁺ also reveal the Fe^{IV}-oxo adduct as the more rapid oxidant in CPET reactions.⁸⁷ This ordering is reversed for cyclohexane oxidation by Fe^{IV}-oxo and Mn^{IV}-oxo adducts of the Bn-TPEN ligand (*k*₂ = 3.9 × 10⁻⁴ and 3.3 × 10⁻³ M⁻¹s⁻¹ for [Fe^{IV}(O)(Bn-TPEN)]²⁺ and [Mn^{IV}(O)(Bn-TPEN)]²⁺, respectively; see Figure 19).^{25, 113} Therefore, no general claim can be made regarding whether Fe^{IV}-oxo or Mn^{IV}-oxo adducts are better at attacking C–H bonds; the answer depends on the supporting ligand.

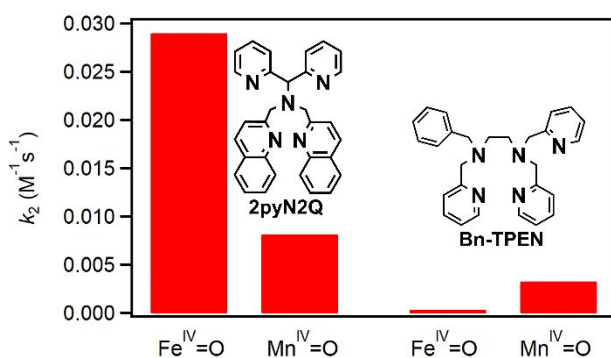


Figure 19. Comparison of second-order rate constants (*k*₂) for cyclohexane oxidation by Fe^{IV}-oxo and Mn^{IV}-oxo adducts supported by 2pyN2Q (left) and Bn-TPEN (right) ligands.

To add even more complexity, the reactivity ordering of [Fe^{IV}(O)(Bn-TPEN)]²⁺ and [Mn^{IV}(O)(Bn-TPEN)]²⁺ depends upon the identity of the substrate. As shown in Figure 20, plots of ln(*k*₂') versus substrate C–H bond dissociation enthalpy for hydrocarbon oxidation by [Fe^{IV}(O)(Bn-TPEN)]²⁺ and [Mn^{IV}(O)(Bn-TPEN)]²⁺ show a crossing point near 90 kcal mol⁻¹ (*k*₂' is the second-order rate constant divided by the number of equivalent C–H bonds).²⁶ The Mn^{IV}-oxo adduct has the faster

rates for substrates with strong C–H bonds but has slower rates for substrates with weaker C–H bonds. The basis for this crossing comes from the more shallow dependence of reaction rate on substrate bond strength for the Mn^{IV}-oxo complex. The slope of the best-fit line of the ln(*k*₂') versus substrate C–H bond dissociation enthalpy plot can be multiplied by $-RT$ to give the unitless Brønsted α parameter, which is 0.19 for [Mn^{IV}(O)(Bn-TPEN)]²⁺ and 0.35 for [Fe^{IV}(O)(Bn-TPEN)]²⁺. (The true α comes from a plot of ΔG^\ddagger vs. ΔG° . Here we rely on the assumption of small, or systematic, variations in entropy for reactions with different substrates.) Small Brønsted α parameters were also observed for hydrocarbon oxidation by [Mn^{IV}(O)(2pyN2Q)]²⁺ (α = 0.24) and [Mn^{IV}(O)₂(Me₂EBC)] (α = 0.21).^{26, 76} More data are needed to determine if a small α is a common feature of Mn^{IV}-oxo species.

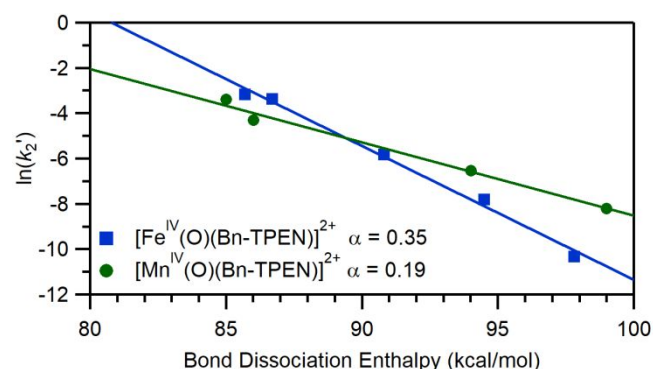


Figure 20. Rates (as ln(*k*₂') of C–H bond oxidation by [Fe^{IV}(O)(Bn-TPEN)]²⁺ and [Mn^{IV}(O)(Bn-TPEN)]²⁺ as a function of calculated substrate bond dissociation energy. The α parameters were obtained by the product of the slopes of best-fit lines (solid lines) and $-RT$. Rate constants are from refs. ¹¹³ (Fe) and ²⁵ (Mn) and the calculated substrate bond enthalpies are from ref. ²⁶.

When the Marcus theory of electron transfer is applied to CPET reactions, a Brønsted α of ca. 0.5 is predicted in cases of small driving force (*i.e.*, $|\Delta G^\circ| \ll 2\lambda$, where ΔG° is the free energy of reaction at standard state and λ is the reorganization energy).²⁷ The difference in α between [Mn^{IV}(O)(Bn-TPEN)]²⁺ and [Fe^{IV}(O)(Bn-TPEN)]²⁺ thus could reflect a difference in driving force regimes; however, a small α would reflect a large driving force,¹²³ which seems unlikely for oxidation of strong C–H bonds by [Mn^{IV}(O)(Bn-TPEN)]²⁺. (Although it must be emphasized that the lack of information concerning the total driving forces for these reactions presents a limitation in this analysis.)

Values of α ranging from 0.10 – 0.7 have been observed for CPET reactions involving a variety of metal oxidants.^{48, 71, 87, 124-127} To the best of our knowledge, there is no consensus basis for understanding these variations, although there are several proposed rationales for unusually low values. An unusually small Brønsted α of 0.08 was observed in hydrocarbon oxidation by a Mn^{III}-hydroxo complex.⁴⁸ This value was tentatively attributed to an asynchronous transition-state, where structural and electronic reorganization of the Mn^{III} centre trails behind hydrogen-atom transfer.⁴⁸ More recently, hydrocarbon oxidation by a Co^{III}-oxo complex¹²⁸ revealed no clear relationship between the reaction barrier ($\log(k_{\text{obs}})$, where

k_{obs} is a pseudo-first-order rate constant) and substrate bond dissociation energy, but a correlation was observed between the reaction barrier and the pK_a of the substrate C–H bond.¹²⁹ These observations were explained in terms of an asynchronous CPET mechanism, where the transition-state carries large proton-transfer character, with electron-transfer trailing behind. Asynchronous behaviour has been proposed in other CPET reactions, in some cases to rationalize a small Brønsted α .^{130–132} Methods of using thermodynamic parameters to evaluate asynchronous CPET reactions have been reported and applied to Fe^{IV}-oxo systems.¹³³

While such an analysis could prove useful in understanding differences in α between $[\text{Fe}^{\text{IV}}(\text{O})(\text{Bn-TPEN})]^{2+}$ and $[\text{Mn}^{\text{IV}}(\text{O})(\text{Bn-TPEN})]^{2+}$ (Figure 20), the concept of asynchronous CPET has been called into question,¹²³ particularly in cases where proton tunnelling contributes to the reaction rate.¹³⁴ The Marcus treatment of CPET from which predictions of a Brønsted α of ca. 0.5 derives does not properly account for proton tunnelling contributions.²⁷ As there is experimental evidence for proton tunnelling for $[\text{Fe}^{\text{IV}}(\text{O})(\text{N4py})]^{2+}$ and $[\text{Mn}^{\text{IV}}(\text{O})(\text{N4py})]^{2+}$,^{34, 121} a theoretical model incorporating proton quantum effects is needed to fully understand variations in Brønsted α in CPET reactions for Fe^{IV}-oxo and Mn^{IV}-oxo centres. Alternatively, a change in mechanism as a function of driving force (from CPET to stepwise PTET or ETPT) could also account for deviations in α in from 0.5.¹²³ In any case, more experimental comparisons of Fe^{IV}-oxo and Mn^{IV}-oxo centres at parity of coordination sphere and, ideally at parity of solvent, are necessary to fully elaborate on the similarities and distinctions between these oxidants.

One final caveat in comparing the reactivity of these metal-oxo species is the difference in solvent used for the reactions. For the Mn^{IV}-oxo species, CF₃CH₂OH is required as a solvent or co-solvent;^{25, 82} thus, most kinetic investigations are in pure CF₃CH₂OH or 50:50 CF₃CH₂OH:CH₂Cl₂.^{25, 34, 35, 82, 87} In contrast, the majority of the kinetic studies for the Fe^{IV}-oxo systems have been performed in MeCN.^{91, 113} As we have discussed,²⁶ the limited data available comparing Fe^{IV}-oxo reactivity in CF₃CH₂OH and MeCN show that reactions with hydrocarbons are faster in CF₃CH₂OH,^{87, 113} but this effect appears to be dampened as the substrate C–H bond strength increases.

Outlook

Recent years have seen remarkable advances in our understanding of the influences of geometric and electronic structure on the reactivity of Mn^{III}-hydroxo and Mn^{IV}-oxo adducts. At the beginning of 2014, just one Mn^{III}-hydroxo adduct known to attack C–H bonds had been reported;⁴⁸ now there are families of Mn^{III}-hydroxo adducts, with a variety of ligand types.^{54, 66, 135, 136} Several of these complexes can oxidize weak C–H bonds. The report by Nam and co-workers in 2011 of a Mn^{IV}-oxo complex capable of oxidizing the strong C–H bond of cyclohexane²⁵ spawned a computationally-derived multi-state reactivity model³⁶ that inspired the development of even more reactive Mn^{IV}-oxo adducts.^{26, 35} This multi-state reactivity model has been probed through combined experimental and computational studies.^{86, 87}

The reactivity of the Mn^{III}-hydroxo unit of $[\text{Mn}^{\text{III}}(\text{OH})(\text{dpaq})]^{+}$ in CPET reactions can be controlled by modifying electron donation to the Mn^{III}-hydroxo adduct from the supporting ligand.⁶⁶ In this case, changes in the Mn^{III/II} reduction potential correlated with the observed variation in reactivity. Complementary investigations of Mn^{III}-oxo complexes (the conjugate base of a Mn^{III}-hydroxo adduct) have shown that modulation of hydrogen-bond donors to the Mn^{III}-oxo adduct affects the basicity of the oxo ligand.¹³⁵ For these systems, the change in Mn^{III}-oxo basicity was correlated with changes in C–H bond oxidation rates. The studies of both the Mn^{III}-hydroxo and Mn^{III}-oxo complexes reveal the seeming inevitability of compensation, where changes in metal ion potential and metal-ligand (ligand = oxo or hydroxo) basicity shift in opposing directions upon ligand modifications. Similar observations were made for Cu^{III}-hydroxo complexes.⁷¹ An important question is - what governs if changes in potential or basicity are dominant? To date, Mn^{III}-hydroxo adducts have served as outstanding model systems for understanding intimate details of CPET reactions; we hope that future studies will continue to address fundamental questions in this field.

While Mn^{IV}-oxo adducts are now known to be capable of attacking strong C–H bonds, significant advances for these systems are required to make them suitable for catalytic applications. The most reactive Mn^{IV}-oxo complexes are generated using iodosobenzene, which has poor atom economy. The formation of these Mn^{IV}-oxo complexes also requires CF₃CH₂OH as a solvent or co-solvent.^{25, 82} The basis for the status of CF₃CH₂OH as a privileged solvent is unclear, but a role in stabilizing the Mn^{IV}-oxo unit through hydrogen-bonding was proposed.⁹⁰ This proposal requires further evaluation. In some cases cerium(IV) ammonium nitrate has been used to generate Mn^{IV}-oxo adducts in non-fluorinated solvents.¹³⁷ While intriguing from a fundamental perspective, this oxidant is not atom economical.

Even with the use of a non-fluorinated solvent and a more atom economical oxidant, Mn^{IV}-oxo centers would still present an additional challenge for catalytic applications. Stoichiometric investigations of hydrocarbon oxidation by $[\text{Mn}^{\text{IV}}(\text{O})(\text{Bn-TPEN})]^{2+}$ and $[\text{Mn}^{\text{IV}}(\text{O})(\text{N4py})]^{2+}$ each revealed the formation of ca. 0.5 equiv. organic product per equiv. of Mn^{IV}-oxo consumed.^{25, 34} Further analysis revealed the formation of a Mn^{III} complex as the primary Mn-based product. These observations suggest a mechanism where one Mn^{IV}-oxo center abstracts a hydrogen atom from substrate to give a Mn^{III}-hydroxo product and the substrate radical. Instead of a rebound step, which would result in hydroxylated product, the substrate radical diffuses from the Mn^{III}-hydroxo complex and is attacked by a second Mn^{IV}-oxo complex to give the desaturated product and a second equiv. of Mn^{III}-hydroxo complex. This so-called non-rebound mechanism¹³⁸ thwarts catalytic applications, as the Mn^{II} starting complex is not regenerated. Ligand design might be one potential method of over-coming this drawback. For example, the reaction of $[\text{Mn}^{\text{II}}(2\text{pyN2Q})(\text{OTf})](\text{OTf})$ with an excess of PhIO and cyclohexane under an inert atmosphere showed the formation of 3.5(5) equiv. cyclohexanol.²⁶ These results offer some partial support for a rebound mechanism,

which might be more favorable for the 2pyN2Q ligand than the N4py ligand. While the basis for this change in rebound favorability is uncertain, recent experiments by Goldberg and co-workers at probing rebound reactions of Fe^{III}-hydroxo and Fe^{III}-methoxy centers¹³⁹⁻¹⁴¹ could lead to a greater understanding of these important functionalization steps that occur after the initial substrate attack by a CPET step.

A far more appealing method for the generation of a Mn^{IV}-oxo adduct would be by O₂ activation, as proposed for some Mn^{II} complexes (Figure 9). In these cases bulky ligands prevent the formation of oxo-bridged dimanganese(III,III) species. These systems would still pose a problem for catalysts, as a Mn^{III}-hydroxo adduct, and not the Mn^{II} starting material is the terminal product. In addition, these O₂-activating Mn^{II} complexes have not been capable of performing synthetically interesting aerobic oxidation reactions even under stoichiometric conditions.⁶⁷ This result is curious, as the incorporation of deuterium in the Mn^{III}-hydroxo product observed upon oxygenation of [Mn^{II}(dpaq^{2Me})](OTf) in d₃-MeCN requires the formation of an oxidant with the ability to attack a kinetically inert C–H(D) bond.⁶⁷ In general, understanding of O₂ activation by Mn^{II} centres lags behind that of Fe^{II} and Cu^I systems, and future research in this area should be fruitful.

While this review has underscored the high reactivity of certain Mn^{IV}-oxo complexes, Mn^V-oxo units are presumptive oxidants in many Mn catalysts.²¹ However, there is a disconnection between the high reactivity of these catalysts and the modest reactivity of many synthetically isolable Mn^V-oxo centres. Although there are many differences between the Mn^V-oxo complexes and those presumed to form for certain catalysts, recent work has brought attention to the importance of spin state for Mn^V-oxo complexes. The majority of Mn^V-oxo centres are in tetragonal environments and have *S* = 0 ground states. Utilizing a C₃-symmetric ligand with a hydrogen-bonding cavity, Borovik and co-workers generated a Mn^V-oxo complex with an *S* = 1 ground state.^{18, 19} Both EPR and Mn Kβ X-ray emission spectroscopies verified the *S* = 1 Mn^V assignment.¹⁹ These studies established the spectroscopic properties of a *bona fide* high-spin Mn^V-oxo adduct, but, to the best of our knowledge, no reactivity studies have been reported. Nam, Sun, and co-workers invoked the importance of spin state to understand catalytic hydrocarbon oxidation by [Mn^{II}(S-PMB)]²⁺ (S-PMB = (S)-*N*-methyl-1-(1-methyl-1H-benzo-[d]imidazol-2-yl)-*N*-((1-(1-methyl-1H-benzo[d]imidazol-2-yl)methyl)pyrrolidin-2-yl)-methyl)methanamine).²⁴ Experimental and computational results suggest that an *S* = 1 [Mn^V(O)(OAc)(S-PMB)]²⁺ complex should be more reactive for hydrocarbon oxidation than its *S* = 0 analogue.²⁴ These and other studies described in this Feature underscore the richness of oxidation reactions of Mn-oxo and Mn-hydroxo adducts and should serve as inspiration for years to come.

Conflicts of interest

There are no conflicts to declare.

Acknowledgements

We thank all our past co-workers and collaborators who have made important contributions to this work on manganese model complexes. In particular, we thank Dr. Ebbe Nordlander (Lund University, Sweden) for his long-standing collaboration on Mn^{IV}-oxo complexes. Our work on Mn^{III}-hydroxo complexes is presently supported by the U.S. NSF (CHE-1900384); our work on Mn^{IV}-oxo adducts is supported by the U.S. DOE (DE-SC0016359). J. Mayfield is supported by the National Institutes of Health Graduate Training Program in Dynamic Aspects of Chemical Biology (Grant T32 1001147 from NIGMS).

Notes and references

- M. A. Zoroddu, J. Aaseth, G. Crisponi, S. Medici, M. Peana and V. M. Nurchi, *J. Inorg. Biochem.*, 2019, **195**, 120-129.
- D. F. Leto and T. A. Jackson, *J. Biol. Inorg. Chem.*, 2014, **19**, 1-15.
- J. Yano and V. Yachandra, *Chem. Rev.*, 2014, **114**, 4175-4205.
- W. Zhu and N. G. J. Richards, *Essays In Biochemistry*, 2017, **61**, 259-270.
- Y. Sheng, I. A. Abreu, D. E. Cabelli, M. J. Maroney, A.-F. Miller, M. Teixeira and J. S. Valentine, *Chem. Rev.*, 2014, **114**, 3854-3918.
- D. B. Rice, A. A. Massie and T. A. Jackson, *Acc. Chem. Res.*, 2017, **50**, 2706-2717.
- X. Engelmann, I. Monte-Perez and K. Ray, *Angew. Chem., Int. Ed.*, 2016, **55**, 7632-7649.
- K. Ray, F. F. Pfaff, B. Wang and W. Nam, *J. Am. Chem. Soc.*, 2014, **136**, 13942-13958.
- A. Company, J. Lloret-Fillol and M. Costas, *Comprehensive Inorganic Chemistry II (Second Edition): From Elements to Applications*, 2013, **3**, 487-564.
- A.-F. Miller, *FEBS Lett.*, 2012, **586**, 585-595.
- T. A. Jackson and T. C. Brunold, *Acc. Chem. Res.*, 2004, **37**, 461-470.
- R. A. Baglia, J. P. T. Zaragoza and D. P. Goldberg, *Chem. Rev.*, 2017, **117**, 13320-13352.
- H. M. Neu, R. A. Baglia and D. P. Goldberg, *Acc. Chem. Res.*, 2015, **48**, 2754-2764.
- M. Guo, T. Corona, K. Ray and W. Nam, *ACS Central Science*, 2019, **5**, 13-28.
- J. J. D. Sacramento and D. P. Goldberg, *Acc. Chem. Res.*, 2018, **51**, 2641-2652.
- H. R. Rose, M. K. Ghosh, A. O. Maggiolo, C. J. Pollock, E. J. Blaes, V. Hajj, Y. Wei, L. J. Rajakovich, W.-c. Chang, Y. Han, M. Hajj, C. Krebs, A. Silakov, M.-E. Pandelia, J. M. Bollinger and A. K. Boal, *Biochemistry*, 2018, **57**, 2679-2693.
- R. D. Britt, D. L. M. Suess and T. A. Stich, *Proc. Natl. Acad. Sci. U.S.A.*, 2015, **112**, 5265-5266.
- R. Gupta, T. Taguchi, B. Lassalle-Kaiser, E. L. Bominaar, J. Yano, M. P. Hendrich and A. S. Borovik, *Proc. Natl. Acad. Sci. U.S.A.*, 2015, **112**, 5319-5324.
- T. Taguchi, R. Gupta, B. Lassalle-Kaiser, D. W. Boyce, V. K. Yachandra, W. B. Tolman, J. Yano, M. P. Hendrich and A. S. Borovik, *J. Am. Chem. Soc.*, 2012, **134**, 1996-1999.
- M. Milan, M. Salamone, M. Costas and M. Bietti, *Acc. Chem. Res.*, 2018, **51**, 1984-1995.
- R. V. Ottenbacher, E. P. Talsi and K. P. Bryliakov, *The Chemical Record*, 2018, **18**, 78-90.

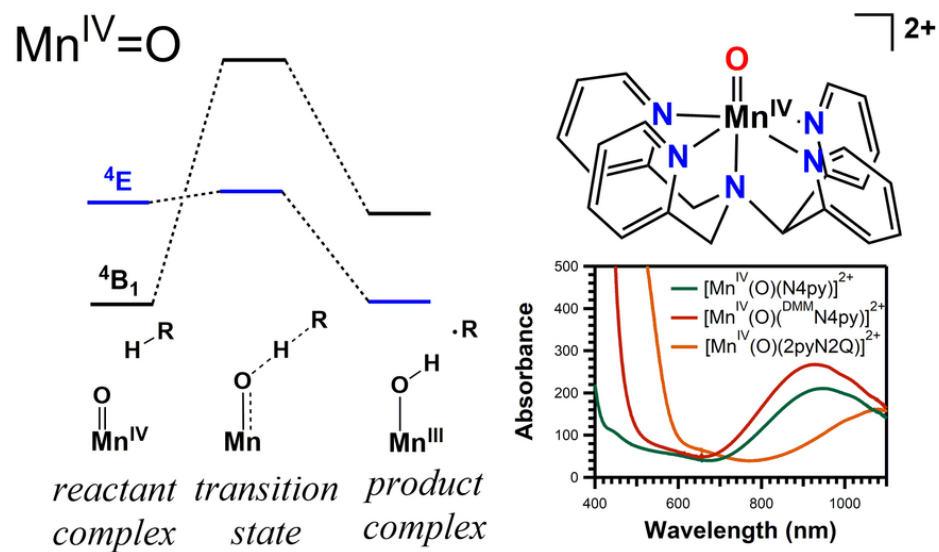
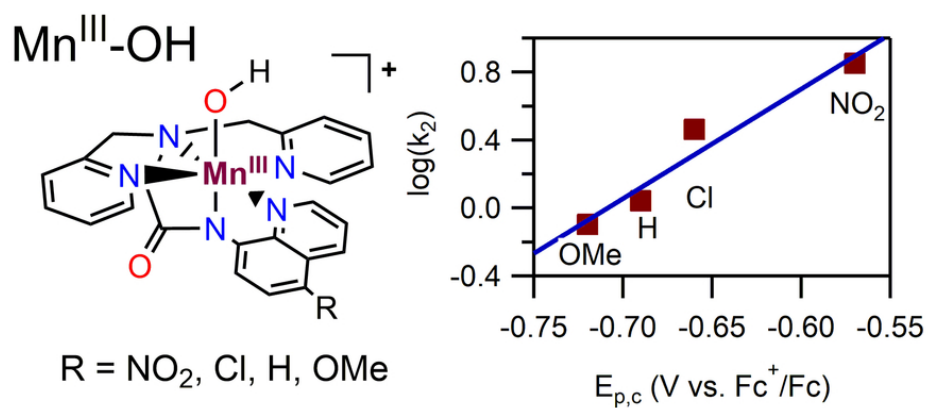
22. W. Sun and Q. Sun, *Acc. Chem. Res.*, 2019, **52**, 2370-2381.
23. M. C. White and J. Zhao, *J. Am. Chem. Soc.*, 2018, **140**, 13988-14009.
24. X.-X. Li, M. Guo, B. Qiu, K.-B. Cho, W. Sun and W. Nam, *Inorg. Chem.*, 2019, **58**, 14842-14852.
25. X. Wu, M. S. Seo, K. M. Davis, Y.-M. Lee, J. Chen, K.-B. Cho, Y. N. Pushkar and W. Nam, *J. Am. Chem. Soc.*, 2011, **133**, 20088-20091.
26. A. A. Massie, A. Sinha, J. D. Parham, E. Nordlander and T. A. Jackson, *Inorg. Chem.*, 2018, **57**, 8253-8263.
27. J. W. Darcy, B. Koronkiewicz, G. A. Parada and J. M. Mayer, *Acc. Chem. Res.*, 2018, **51**, 2391-2399.
28. S. Hammes-Schiffer, *Chem. Rev.*, 2010, **110**, 6937-6938.
29. J. P. Layfield and S. Hammes-Schiffer, *Chem. Rev.*, 2014, **114**, 3466-3494.
30. P. Pirovano and A. R. McDonald, *Eur. J. Inorg. Chem.*, 2018, 547-560.
31. D. B. Rice, S. D. Jones, J. T. Douglas and T. A. Jackson, *Inorg. Chem.*, 2018, **57**, 7825-7837.
32. D. B. Rice, G. B. Wijeratne, A. D. Burr, J. D. Parham, V. W. Day and T. A. Jackson, *Inorg. Chem.*, 2016, **55**, 8110-8120.
33. G. B. Wijeratne, B. Corzine, V. W. Day and T. A. Jackson, *Inorg. Chem.*, 2014, **53**, 7622-7634.
34. D. F. Leto, R. Ingram, V. W. Day and T. A. Jackson, *Chem. Commun.*, 2013, **49**, 5378-5380.
35. A. A. Massie, M. C. Denler, L. T. Cardoso, A. N. Walker, M. K. Hossain, V. W. Day, E. Nordlander and T. A. Jackson, *Angew. Chem. Int. Ed.*, 2017, **56**, 4178-4182.
36. K.-B. Cho, S. Shaik and W. Nam, *The Journal of Physical Chemistry Letters*, 2012, **3**, 2851-2856.
37. A. Wennman, E. H. Oliw, S. Karkehabadi and Y. Chen, *Journal of Biological Chemistry*, 2016, **291**, 8130-8139.
38. C. Su and E. H. Oliw, *J. Biol. Chem.*, 1998, **273**, 13072-13079.
39. C. Su, M. Sahlin and E. H. Oliw, *J. Biol. Chem.*, 2000, **275**, 18830-18835.
40. A. Wennman, S. Karkehabadi and E. H. Oliw, *Arch. Biochem. Biophys.*, 2014, **555-556**, 9-15.
41. E. H. Oliw, *Journal of Lipid Research*, 2008, **49**, 420-428.
42. E. H. Oliw, F. Jernerén, I. Hoffmann, M. Sahlin and U. Garscha, *Biochimica et Biophysica Acta (BBA) - Molecular and Cell Biology of Lipids*, 2011, **1811**, 138-147.
43. E. H. Oliw, A. Wennman, I. Hoffmann, U. Garscha, M. Hamberg and F. Jernerén, *Journal of Lipid Research*, 2011, **52**, 1995-2004.
44. N. Lehnert and E. I. Solomon, *J Biol Inorg Chem*, 2003, **8**, 294-305.
45. D. M. Eichhorn and W. H. Armstrong, *J. Chem. Soc., Chem. Commun.*, 1992, 85-87.
46. S. El Ghachtouli, B. Lassalle-Kaiser, P. Dorlet, R. Guillot, E. Anxolabehere-Mallart, C. Costentin and A. Aukauloo, *Energy & Environmental Science*, 2011, **4**, 2041-2044.
47. A. A. Eroy-Reveles, Y. Leung, C. M. Beavers, M. M. Olmstead and P. K. Mascharak, *J. Am. Chem. Soc.*, 2008, **130**, 4447-4458.
48. C. R. Goldsmith, A. P. Cole and T. D. P. Stack, *J. Am. Chem. Soc.*, 2005, **127**, 9904-9912.
49. T. J. Hubin, J. M. McCormick, N. W. Alcock and D. H. Busch, *Inorg. Chem.*, 2001, **40**, 435-444.
50. Z. Shirin, B. S. Hammes, V. G. Young and A. S. Borovik, *J. Am. Chem. Soc.*, 2000, **122**, 1836-1837.
51. Z. Shirin, A. S. Borovik and V. G. Young Jr, *Chem. Commun.*, 1997, 1967-1968.
52. J. J. Warren, T. A. Tronic and J. M. Mayer, *Chem. Rev.*, 2010, **110**, 6961-7001.
53. J. M. Mayer, *Acc. Chem. Res.*, 2011, **44**, 36-46.
54. M. K. Coggins, L. M. Brines and J. A. Kovacs, *Inorg. Chem.*, 2013, **52**, 12383-12393.
55. M. Sankaralingam, Y.-M. Lee, D. G. Karmalkar, W. Nam and S. Fukuzumi, *J. Am. Chem. Soc.*, 2018, **140**, 12695-12699.
56. D. B. Rice, G. B. Wijeratne and T. A. Jackson, *J Biol Inorg Chem*, 2017, **22**, 1281-1293.
57. K. Ghosh, A. A. Eroy-Reveles, M. M. Olmstead and P. K. Mascharak, *Inorg. Chem.*, 2005, **44**, 8469-8475.
58. J. A. Bonadies, M. J. Maroney and V. L. Pecoraro, *Inorg. Chem.*, 1989, **28**, 2044-2051.
59. Y. Ciringh, S. W. Gordon-Wylie, R. E. Norman, G. R. Clark, S. T. Weintraub and C. P. Horwitz, *Inorg. Chem.*, 1997, **36**, 4968-4982.
60. J. E. Sheats, R. S. Czernuszewicz, G. C. Dismukes, A. L. Rheingold, V. Petrouleas, J. Stubbe, W. H. Armstrong, R. H. Beer and S. J. Lippard, *J. Am. Chem. Soc.*, 1987, **109**, 1435-1444.
61. R. C. Holz, J. M. Bradshaw and B. Bennett, *Inorg. Chem.*, 1998, **37**, 1219-1225.
62. R. C. Holz, J. M. Brink and R. A. Rose, *Journal of Magnetic Resonance, Series A*, 1996, **119**, 125-128.
63. A. Asokan and P. T. Manoharan, *Inorg. Chem.*, 1999, **38**, 5642-5654.
64. C. A. Kipke, M. J. Scott, J. W. Gohdes and W. H. Armstrong, *Inorg. Chem.*, 1990, **29**, 2193-2194.
65. O. Horner, E. Anxolabéhère-Mallart, M. F. Charlot, L. Tchertanov, J. Guilhem, T. A. Mattioli, A. Boussac and J. J. Girerd, *Inorg. Chem.*, 1999, **38**, 1222-1232.
66. D. B. Rice, A. Munasinghe, E. N. Grottemeyer, A. D. Burr, V. W. Day and T. A. Jackson, *Inorg. Chem.*, 2019, **58**, 622-636.
67. J. D. Parham, G. B. Wijeratne, J. R. Mayfield and T. A. Jackson, *Dalton Trans.*, 2019, **48**, 13034-13045.
68. M. K. Coggins, X. Sun, Y. Kwak, E. I. Solomon, E. Rybak-Akimova and J. A. Kovacs, *J. Am. Chem. Soc.*, 2013, **135**, 5631-5640.
69. Y. Hitomi, Y. Iwamoto and M. Kodera, *Dalton Trans.*, 2014, **43**, 2161-2167.
70. B. H. Solis and S. Hammes-Schiffer, *Inorg. Chem.*, 2014, **53**, 6427-6443.
71. D. Dhar, G. M. Yee, A. D. Spaeth, D. W. Boyce, H. Zhang, B. Dereli, C. J. Cramer and W. B. Tolman, *J. Am. Chem. Soc.*, 2016, **138**, 356-368.
72. D. B. Rice, E. N. Grottemeyer, A. M. Donovan and T. A. Jackson, *Inorg. Chem.*, 2020, **59**, 2689-2700.
73. T. H. Parsell, R. K. Behan, M. T. Green, M. P. Hendrich and A. S. Borovik, *J. Am. Chem. Soc.*, 2006, **128**, 8728-8729.
74. T. H. Parsell, M.-Y. Yang and A. S. Borovik, *J. Am. Chem. Soc.*, 2009, **131**, 2762-2763.
75. T. Kurahashi, A. Kikuchi, Y. Shiro, M. Hada and H. Fujii, *Inorg. Chem.*, 2010, **49**, 6664-6672.
76. G. Yin, A. M. Danby, D. Kitko, J. D. Carter, W. M. Scheper and D. H. Busch, *J. Am. Chem. Soc.*, 2008, **130**, 16245-16253.
77. I. Garcia-Bosch, A. Company, C. W. Cady, S. Styring, W. R. Browne, X. Ribas and M. Costas, *Angew. Chem. Int. Ed.*, 2011, **50**, 5648-5653.
78. S. Shi, Y. Wang, A. Xu, H. Wang, Z. Dajian, S. B. Roy, T. A. Jackson, D. H. Busch and G. Yin, *Angew. Chemie Int. Ed.*, 2011, **50**, 7321-7324.
79. M. Puri and L. Que, Jr., *Acc. Chem. Res.*, 2015, **48**, 2443-2452.
80. D. Usharani, D. Janardanan, C. Li and S. Shaik, *Acc. Chem. Res.*, 2013, **46**, 471-482.
81. M. Srncic, S. D. Wong and E. I. Solomon, *Dalton Trans.*, 2014, **43**, 17567-17577.

82. J. Chen, Y.-M. Lee, K. M. Davis, X. Wu, M. S. Seo, K.-B. Cho, H. Yoon, Y. J. Park, S. Fukuzumi, Y. N. Pushkar and W. Nam, *J. Am. Chem. Soc.*, 2013, **135**, 6388-6391.
83. J. Chen, K.-B. Cho, Y.-M. Lee, Y. H. Kwon and W. Nam, *Chemical Communications*, 2015, **51**, 13094-13097.
84. F. Neese and E. I. Solomon, *Inorg. Chem.*, 1999, **38**, 1847-1865.
85. D. F. Leto, A. A. Massie, D. B. Rice and T. A. Jackson, *J. Am. Chem. Soc.*, 2016, **138**, 15413-15424.
86. D. B. Rice, A. A. Massie and T. A. Jackson, *Inorg. Chem.*, 2019, **58**, 13902-13916.
87. J. Chen, K.-B. Cho, Y.-M. Lee, Y. H. Kwon and W. Nam, *Chem. Commun.*, 2015, **51**, 13094-13097.
88. D. Usharani, D. C. Lacy, A. S. Borovik and S. Shaik, *J. Am. Chem. Soc.*, 2013, **135**, 17090-17104.
89. C. Kupper, B. Mondal, J. Serrano-Plana, I. Klawitter, F. Neese, M. Costas, S. Ye and F. Meyer, *J. Am. Chem. Soc.*, 2017, **139**, 8939-8949.
90. A. A. Massie, M. C. Denler, R. Singh, A. Sinha, E. Nordlander and T. A. Jackson, *Chem. Eur. J.*, 2020, **26**, 900-912.
91. W. Rasheed, A. Draksharapu, S. Banerjee, V. G. Young, R. Fan, Y. Guo, M. Ozerov, J. Nehrkorn, J. Krzystek, J. Telsner and L. Que, *Angew. Chem. Int. Ed.*, 2018, **57**, 9387-9391.
92. M. Mitra, H. Nimir, S. Demeshko, S. S. Bhat, S. O. Malinkin, M. Haukka, J. Lloret-Fillol, G. C. Lisensky, F. Meyer, A. A. Shteinman, W. R. Browne, D. A. Hrovat, M. G. Richmond, M. Costas and E. Nordlander, *Inorg. Chem.*, 2015, **54**, 7152-7164.
93. M. C. Denler, A. A. Massie, R. Singh, E. Stewart-Jones, A. Sinha, V. W. Day, E. Nordlander and T. A. Jackson, *Dalton Trans.*, 2019, **48**, 5007-5021.
94. D. F. Leto and T. A. Jackson, *Inorg. Chem.*, 2014, **53**, 6179-6194.
95. J. Chen, H. Yoon, Y.-M. Lee, M. S. Seo, R. Sarangi, S. Fukuzumi and W. Nam, *Chem. Sci.*, 2015, **6**, 3624-3632.
96. N. Sharma, Y.-M. Lee, X.-X. Li, W. Nam and S. Fukuzumi, *Inorg. Chem.*, 2019, **58**, 13761-13765.
97. T. Devi, Y.-M. Lee, W. Nam and S. Fukuzumi, *Coord. Chem. Rev.*, 2020, **410**, 213219.
98. H. Yoon, Y.-M. Lee, X. Wu, K.-B. Cho, R. Sarangi, W. Nam and S. Fukuzumi, *J. Am. Chem. Soc.*, 2013, **135**, 9186-9194.
99. Y.-M. Lee, S. Kim, K. Ohkubo, K.-H. Kim, W. Nam and S. Fukuzumi, *J. Am. Chem. Soc.*, 2019, **141**, 2614-2622.
100. J. Jung, S. Kim, Y.-M. Lee, W. Nam and S. Fukuzumi, *Angew. Chem. Int. Ed.*, 2016, **55**, 7450-7454.
101. S. Kim, K.-B. Cho, Y.-M. Lee, J. Chen, S. Fukuzumi and W. Nam, *J. Am. Chem. Soc.*, 2016, **138**, 10654-10663.
102. N. Sharma, J. Jung, K. Ohkubo, Y.-M. Lee, M. E. El-Khouly, W. Nam and S. Fukuzumi, *J. Am. Chem. Soc.*, 2018, **140**, 8405-8409.
103. M. Sankaralingam, Y.-M. Lee, Y. Pineda-Galvan, D. G. Karmalkar, M. S. Seo, S. H. Jeon, Y. Pushkar, S. Fukuzumi and W. Nam, *J. Am. Chem. Soc.*, 2019, **141**, 1324-1336.
104. D. G. Karmalkar, M. Sankaralingam, M. S. Seo, R. Ezhov, Y.-M. Lee, Y. N. Pushkar, W.-S. Kim, S. Fukuzumi and W. Nam, *Angew. Chem. Int. Ed.*, 2019, **58**, 16124-16129.
105. R. A. Baglia, C. M. Krest, T. Yang, P. Leeladee and D. P. Goldberg, *Inorg. Chem.*, 2016, **55**, 10800-10809.
106. P. Leeladee, R. A. Baglia, K. A. Prokop, R. Latifi, S. P. de Visser and D. P. Goldberg, *J. Am. Chem. Soc.*, 2012, **134**, 10397-10400.
107. C. J. Bougher, S. Liu, S. D. Hicks and M. M. Abu-Omar, *J. Am. Chem. Soc.*, 2015, **137**, 14481-14487.
108. C. J. Bougher and M. M. Abu-Omar, *ChemistryOpen*, 2016, **5**, 522-524.
109. R. A. Baglia, M. Dürr, I. Ivanović-Burmazović and D. P. Goldberg, *Inorg. Chem.*, 2014, **53**, 5893-5895.
110. J. P. T. Zaragoza, R. A. Baglia, M. A. Siegler and D. P. Goldberg, *J. Am. Chem. Soc.*, 2015, **137**, 6531-6540.
111. S. Hong, Y.-M. Lee, M. Sankaralingam, A. K. Vardhaman, Y. J. Park, K.-B. Cho, T. Ogura, R. Sarangi, S. Fukuzumi and W. Nam, *J. Am. Chem. Soc.*, 2016, **138**, 8523-8532.
112. D. G. Karmalkar, X.-X. Li, M. S. Seo, M. Sankaralingam, T. Ohta, R. Sarangi, S. Hong and W. Nam, *Chem. Eur. J.*, 2018, **24**, 17927-17931.
113. J. Kaizer, E. J. Klinker, N. Y. Oh, J.-U. Rohde, W. J. Song, A. Stubna, J. Kim, E. Münck, W. Nam and L. Que, Jr., *J. Am. Chem. Soc.*, 2004, **126**, 472-473.
114. S. Rana, A. Dey and D. Maiti, *Chem. Commun.*, 2015, **51**, 14469-14472.
115. D. Unjaroen, R. Gericke, M. Lovisari, D. Nelis, P. Mondal, P. Pirovano, B. Twamley, E. R. Farquhar and A. R. McDonald, *Inorg. Chem.*, 2019, **58**, 16838-16848.
116. P. Barman, A. K. Vardhaman, B. Martin, S. J. Wörner, C. V. Sastri and P. Comba, *Angew. Chem. Int. Ed.*, 2015, **54**, 2095-2099.
117. R. A. Baglia, K. A. Prokop-Prigge, H. M. Neu, M. A. Siegler and D. P. Goldberg, *J. Am. Chem. Soc.*, 2015, **137**, 10874-10877.
118. J. P. T. Zaragoza, D. C. Cummins, M. Q. E. Mubarak, M. A. Siegler, S. P. de Visser and D. P. Goldberg, *Inorg. Chem.*, 2019, **58**, 16761-16770.
119. E. J. Klinker, J. Kaizer, W. W. Brennessel, N. L. Woodrum, C. J. Cramer and L. Que, Jr., *Angew. Chem. Int. Ed.*, 2005, **44**, 3690-3694.
120. R. L. Halbach, D. Gygi, E. D. Bloch, B. L. Anderson and D. G. Nocera, *Chem. Sci.*, 2018, **9**, 4524-4528.
121. E. J. Klinker, S. Shaik, H. Hirao and L. Que, *Angew. Chem. Int. Ed.*, 2009, **48**, 1291-1295.
122. W. Nam, Y.-M. Lee and S. Fukuzumi, *Acc. Chem. Res.*, 2014, **47**, 1146-1154.
123. C. Costentin and J.-M. Savéant, *Chem. Sci.*, 2020, **11**, 1006-1010.
124. C. V. Sastri, J. Lee, K. Oh, Y. J. Lee, J. Lee, T. A. Jackson, H. Hirao, L. Que, Jr., S. Shaik and W. Nam, *Proc. Natl. Acad. Sci. USA*, 2007, **104**, 19181-19186.
125. D. E. Lansky and D. P. Goldberg, *Inorg. Chem.*, 2006, **45**, 5119-5125.
126. P. Pirovano, E. R. Farquhar, M. Swart and A. R. McDonald, *J. Am. Chem. Soc.*, 2016, **138**, 14362-14370.
127. J. R. Bryant and J. M. Mayer, *J. Am. Chem. Soc.*, 2003, **125**, 10351-10361.
128. M. K. Goetz, E. A. Hill, A. S. Filatov and J. S. Anderson, *J. Am. Chem. Soc.*, 2018, **140**, 13176-13180.
129. M. K. Goetz and J. S. Anderson, *J. Am. Chem. Soc.*, 2019, **141**, 4051-4062.
130. T. F. Markle, J. W. Darcy and J. M. Mayer, *Science Advances*, 2018, **4**, eaat5776.
131. G. Qiu and R. R. Knowles, *J. Am. Chem. Soc.*, 2019, **141**, 2721-2730.
132. M. Mandal, C. E. Elwell, C. J. Bouchev, T. J. Zerk, W. B. Tolman and C. J. Cramer, *J. Am. Chem. Soc.*, 2019, **141**, 17236-17244.
133. D. Bím, M. Maldonado-Domínguez, L. Rulišek and M. Srnc, *Proc. Natl. Acad. Sci. U.S.A.*, 2018, **115**, E10287-E10294.
134. T. Liu, R. Tyburski, S. Wang, R. Fernández-Terán, S. Ott and L. Hammarström, *J. Am. Chem. Soc.*, 2019, **141**, 17245-17259.
135. S. K. Barman, J. R. Jones, C. Sun, E. A. Hill, J. W. Ziller and A. S. Borovik, *J. Am. Chem. Soc.*, 2019, **141**, 11142-11150.
136. R. L. Shook, S. M. Peterson, J. Greaves, C. Moore, A. L. Rheingold and A. S. Borovik, *J. Am. Chem. Soc.*, 2011, **133**, 5810-5817.
137. S. C. Sawant, X. Wu, J. Cho, K.-B. Cho, S. H. Kim, M. S. Seo, Y.-M.

ARTICLE

Journal Name

- Lee, M. Kubo, T. Ogura, S. Shaik and W. Nam, *Angew. Chem. Int. Ed.*, 2010, **49**, 8190-8194.
138. K.-B. Cho, H. Hirao, S. Shaik and W. Nam, *Chem. Soc. Rev.*, 2016, **45**, 1197-1210.
139. J. P. T. Zaragoza, T. H. Yosca, M. A. Siegler, P. Moënne-Loccoz, M. T. Green and D. P. Goldberg, *J. Am. Chem. Soc.*, 2017, **139**, 13640-13643.
140. T. M. Pangia, V. Yadav, E. F. Gérard, Y.-T. Lin, S. P. de Visser, G. N. L. Jameson and D. P. Goldberg, *Inorg. Chem.*, 2019, **58**, 9557-9561.
141. V. Yadav, J. B. Gordon, M. A. Siegler and D. P. Goldberg, *J. Am. Chem. Soc.*, 2019, **141**, 10148-10153.



39x40mm (600 x 600 DPI)